REAL-TIME HYBRID EXPERIMENTAL-NUMERICAL SIMULATION OF BRIDGE INFRASTRUCTURE SUBJECT TO CASCADING EARTHQUAKE-TSUNAMI HAZARDS

FINAL PROJECT REPORT

by

Principal Investigator: Barbara G. Simpson
Oregon State University

Sponsorship
PacTrans

for

DISCLAIMER

The contents of this report reflect the views of the authors, who are responsible for the facts and the accuracy of the information presented herein. This document is disseminated under the sponsorship of the U.S. Department of Transportation's University Transportation Centers Program, in the interest of information exchange. The Pacific Northwest Transportation Consortium, the U.S. Government and matching sponsor assume no liability for the contents or use thereof.

TECHNICAL REPORT DOCUMENTATION PAGE

1. Report No.	2. Government Accession No. 01764460	3. Recipient's Catalog No.	
4. Title and Subtitle REAL-TIME HYBRID EXPERIMENTAL-NUMERICAL SIMULATION OF BRIDGE INFRASTRUCTURE SUBJECT TO CASCADING EARTHQUAKE-TSUNAMI HAZARDS		5. Report Date 06/15/2022	
		6. Performing Organization Code	
7. Author(s) and Affiliations Christopher R. Neumann, Oregon State University Barbara G. Simpson, 0000-0002-3661-9548; Oregon State University		8. Performing Organization Report No. 2020-S-OSU-2	
9. Performing Organization Name and Address PacTrans Pacific Northwest Transportation Consortium University Transportation Center for Federal Region 10 University of Washington More Hall 112 Seattle, WA 98195-2700		10. Work Unit No. (TRAIS)	
		11. Contract or Grant No. 69A3551747110	
12. Sponsoring Organization Name and Address United States Department of Transportation Research and Innovative Technology Administration 1200 New Jersey Avenue, SE Washington, DC 20590		13. Type of Report and Period Covered Project draft report, 08/16/20 - 08/15/21	
		14. Sponsoring Agency Code	
15. Supplementary Notes Report uploaded to: www.pactrans.org			

16. Abstract

While real-time hybrid simulation has been utilized for structures subjected to seismic events for decades, its use in fluid-structure interaction problems is still a novel endeavor. Gathering data for cascading seismic and tsunami events is difficult because of space constraints in existing experimental facilities, complications regarding the application of scaling laws for both the fluid and structure, and limitations of computational software in simulating multiple hazards within the same analysis. To alleviate these constraints, this study demonstrated the feasibility of using a real-time hybrid simulation testing method to enhance fluid-structure interaction simulations. A cylindrical bridge pier specimen and three-dimensional numerical bridge model were subjected to cascading seismic and tsunami events within a three-tier, real-time hybrid simulation architecture. The domain was partitioned such that the wave-structure interaction was physically simulated and coupled to a numerical model of the remaining bridge. To simulate existing damage, seismic loading was applied in the structural model before the wave loading. Textbook short pulse response was exhibited by the specimen, and the results illustrated that a real-time hybrid simulation approach is both feasible and economical for future investigations.

17. Key Words real-time hybrid simulation, fluid-structure interaction, multi-hazard, wave impact, tsunami		18. Distribution Statement	
19. Security Classification (of this report) Unclassified.	20. Security Classification (of this page) Unclassified.	21. No. of Pages 44	22. Price N/A

Form DOT F 1700.7 (8-72)   **Reproduction of completed page authorized.**

SI* (MODERN METRIC) CONVERSION FACTORS

APPROXIMATE CONVERSIONS TO SI UNITS

Symbol	When You Know	Multiply By	To Find	Symbol
		LENGTH		
in	inches	25.4	millimeters	mm
ft	feet	0.305	meters	m
yd	yards	0.914	meters	m
mi	miles	1.61	kilometers	km
		AREA		
in^2	square inches	645.2	square millimeters	mm^2
ft^2	square feet	0.093	square meters	m^2
yd^2	square yard	0.836	square meters	m^2
ac	acres	0.405	hectares	ha
mi^2	square miles	2.59	square kilometers	km^2
		VOLUME		
fl oz	fluid ounces	29.57	milliliters	mL
gal	gallons	3.785	liters	L
ft^3	cubic feet	0.028	cubic meters	m^3
yd^3	cubic yards	0.765	cubic meters	m^3
		NOTE: volumes greater than 1000 L shall be shown in m^3		
		MASS		
oz	ounces	28.35	grams	g
lb	pounds	0.454	kilograms	kg
T	short tons (2000 lb)	0.907	megagrams (or "metric ton")	Mg (or "t")
		TEMPERATURE (exact degrees)		
°F	Fahrenheit	5 (F-32)/9 or (F-32)/1.8	Celsius	°C
		ILLUMINATION		
fc	foot-candles	10.76	lux	lx
fl	foot-Lamberts	3.426	candela/m^2	cd/m^2
		FORCE and PRESSURE or STRESS		
lbf	poundforce	4.45	newtons	N
lbf/in^2	poundforce per square inch	6.89	kilopascals	kPa

APPROXIMATE CONVERSIONS FROM SI UNITS

Symbol	When You Know	Multiply By	To Find	Symbol
		LENGTH		
mm	millimeters	0.039	inches	in
m	meters	3.28	feet	ft
m	meters	1.09	yards	yd
km	kilometers	0.621	miles	mi
		AREA		
mm^2	square millimeters	0.0016	square inches	in^2
m^2	square meters	10.764	square feet	ft^2
m^2	square meters	1.195	square yards	yd^2
ha	hectares	2.47	acres	ac
km^2	square kilometers	0.386	square miles	mi^2
		VOLUME		
mL	milliliters	0.034	fluid ounces	fl oz
L	liters	0.264	gallons	gal
m^3	cubic meters	35.314	cubic feet	ft^3
m^3	cubic meters	1.307	cubic yards	yd^3
		MASS		
g	grams	0.035	ounces	oz
kg	kilograms	2.202	pounds	lb
Mg (or "t")	megagrams (or "metric ton")	1.103	short tons (2000 lb)	T
		TEMPERATURE (exact degrees)		
°C	Celsius	1.8C+32	Fahrenheit	°F
		ILLUMINATION		
lx	lux	0.0929	foot-candles	fc
cd/m^2	candela/m^2	0.2919	foot-Lamberts	fl
		FORCE and PRESSURE or STRESS		
N	newtons	0.225	poundforce	lbf
kPa	kilopascals	0.145	poundforce per square inch	lbf/in^2

*SI is the symbol for the International System of Units. Appropriate rounding should be made to comply with Section 4 of ASTM E380.
(Revised March 2003)

TABLE OF CONTENTS

LIST OF FIGURES

vii

LIST OF TABLES

ACKNOWLEDGMENTS

LIST OF ABBREVIATIONS

AASHTO	American Association of State Highway and Transportation Officials
ATS	Adaptive time series
DA	Data-acquisition
FFT	Fast Fourier Transform
GPM	Gallons per minute
LMSR	Large moment-small distance
LWF	Large Wave Flume
LVDT	Linear variable displacement transducer
OS	Operator-splitting
OSU	Oregon State University
PGV	Peak ground velocity
RTHS	Real-time hybrid simulation
RWS	Root-mean-square
SDC	Seismic design criteria
SSI	Soil-structure interaction

EXECUTIVE SUMMARY

While real-time hybrid simulation has been utilized for structures subjected to seismic events for decades, its use in fluid-structure interaction problems is still a novel endeavor. Gathering data for cascading seismic and tsunami events is difficult because of space constraints in existing experimental facilities, complications regarding the application of scaling laws for both the fluid and structure, and limitations of computational software in simulating multiple hazards within the same analysis. To alleviate these constraints, this study demonstrated the feasibility of using a real-time hybrid simulation testing method to enhance fluid-structure interaction simulations. A cylindrical bridge pier specimen and three-dimensional numerical bridge model were subjected to cascading seismic and tsunami events within a three-tier, real-time hybrid simulation architecture. The domain was partitioned such that the wave-structure interaction was physically simulated and coupled to a numerical model of the remaining bridge. To simulate existing damage, seismic loading was applied in the structural model before the wave loading. Textbook short pulse response was exhibited by the specimen, and the results illustrate that a real-time hybrid simulation approach is both feasible and economical for future investigations.

CHAPTER 1. INTRODUCTION

Coastal bridges are critical recovery following natural disasters and provide transportation and access to lifeline systems. Ensuring that bridges are capable of resisting demands due to cascading events, such as earthquakes followed by tsunamis, is crucial to achieving life safety performance objectives and to maintaining access to impacted areas for emergency response, repair, and recovery after extreme events. The 2011 Great East Japan earthquake and resulting Tohoku tsunami resulted in extensive damage to over 300 bridge superstructures (Iemura et al. 2005, Yashinsky 2012). Many of these bridges survived the seismic event but failed because of wave loading from the subsequent tsunami (Akiyama et al. 2012). Multiple mechanisms for failure were observed, including those pertaining to uplift and unseating of bridge spans (Kawashima 2012) and failure of bridge piers (Maruyama et al. 2012). However, although the seismic performance of bridges has been extensively studied over the past few decades (Ketchum et al. 2004, Traubita 2009, Aviram et al. 2012), few data exist on the performance of bridges sequentially subjected to cascading seismic and tsunami events.

Because of spatial constraints in existing hydrodynamic facilities, individual bridge components, such as decks and piers, or small-scale system models are typically used to study wave-structure interaction (Wüthrich et al. 2016, Tomiczek et al. 2016, Park et al. 2017) and bridge behavior (Robertson et al. 2008). However, Froude scaling is often used to model shallow water waves, such as tsunamis, and the similitude of the structural dynamics is often neglected; it is difficult to adequately represent the wave dynamics, structural dynamic properties, and potential for inelastic response using scaled structural models. In particular, incorporating structural damage from previous seismic loading for use in hydrodynamic experiments is challenging because of the small scale of the structural specimen, which often makes it infeasible to scale material properties along with the geometric scale. While it is possible to simulate full-scale bridge models numerically (Yim et al. 2015, Azadbakht and Yim 2016, Azadbakht and Yim 2015), limited software exists that is able to apply both seismic and tsunami loading in a single analysis. Moreover, wave-structure interaction is computationally expensive and subject to modeling uncertainties, requiring experimental validation. Therefore, data regarding the effects of tsunami loading on bridges previously damaged from a seismic event are lacking.

Hybrid simulation is a technique that can alleviate these aforementioned limitations by combining the advantages of numerical and experimental simulations. Hybrid simulation is a

1

testing method that has been used to examine the seismic response of structures for decades (Takanashi et al. 1975, Mahin and Williams 1980, Shing and Mahin 1983) by dividing a domain into experimental and analytical sub-domains, defined here as *physical sub-assemblies* and *numerical sub-assemblies*, respectively; see figure 1-1. The physical sub-assembly comprises a test specimen, e.g., herein the wave loading and a bridge pier. The numerical sub-assembly is a digital model of the remaining domain, e.g., herein the remaining bridge structure. Actuators apply loading in the physical model, and sensors send feedback to the numerical model. Thus, with hybrid simulation, physical and numerical sub-assemblies are coupled, enabling more holistic testing of structures that would otherwise be too large to fit within existing laboratories and/or too expensive to construct in their entirety.
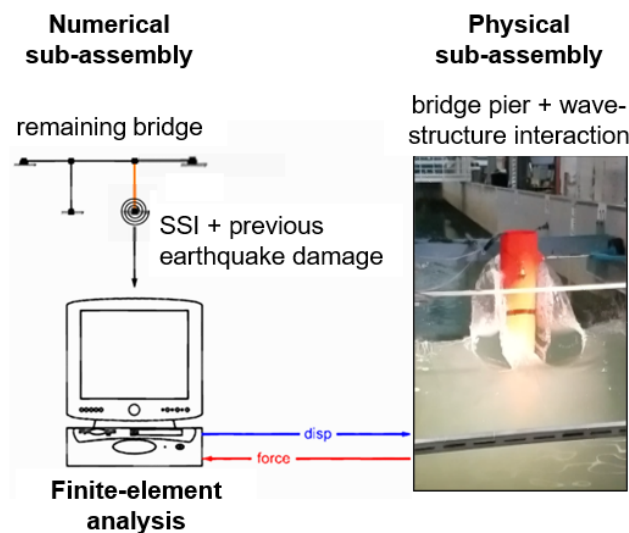
Figure 1-1. Schematic of hydro-RTHS

If the rate of loading plays a significant role in the dynamics of the physical sub-assembly (e.g., with physical water that must flow in real time), the coupling between the numerical and physical sub-assemblies must occur in real time, dubbed *real-time hybrid simulation* (RTHS) (Nakashima et al. 1992). On the physical side, RTHS requires dynamic actuators and high-speed data acquisition systems capable of responding and sampling in real time (Carrion and Spencer 2007). On the numerical side, the computation of each time step in the numerical sub-assembly must be calculated in near-real time (Kolay et al. 2018). Additionally, small-scale models, which are often needed for hydrodynamic experiments, require faster-than-real-time computations to

2

satisfy dynamic similitude requirements. Although a plethora of literature exists pertaining to errors in simulations, integration methods, stability and accuracy, and frameworks for conducting geographically distributed tests for seismic loading (Dorka 2002, Mosqueda 2003, Bayer et al. 2005, Pan et al. 2005, Zhong 2005, Schellenberg et al. 2009, Chae et al. 2013, Kolay et al. 2018), relatively few experiments have studied RTHS for wave-structure interaction problems.

Recent research has applied RTHS to wave-structure interaction problems pertaining to floating offshore wind turbines (Chabaud et al. 2013, Sauder et al. 2016, Hall 2016, Hall and Goupee 2018). Incompatibilities between similitude requirements for waves and wind affecting the wind turbine response have been alleviated by modeling the wave-structure interaction physically and the wind-structure interaction numerically; scaling laws can then be applied separately in the physical and numerical models. The RTHS method has been subsequently generalized for various ocean structures, including simulations with a physical buoy and numerical mooring system (Vilsen et al. 2019). An inverse approach has also been studied, in which the wind was modeled physically in a wind tunnel and the waves were modeled numerically and actuated by using a six degree-of-freedom robotic system (Bayati et al. 2018, La Mura et al. 2018).

This study used RTHS in combination with hydrodynamic loading, termed *hydro-RTHS*, to evaluate the vulnerability of bridges to cascading seismic and tsunami events. As previous work focused on floating structures, this application required significantly larger actuation capacity, so hydraulic actuators were utilized. The domain was partitioned such that the wave-structure interaction was physically simulated and coupled to a numerical model of the remaining bridge; see figure 1-1. The physical sub-assembly included the physical wave loading and a partial structural specimen, representing a single bridge pier, and was located in the Large Wave Flume at the O.H. Hinsdale Wave Research Laboratory at Oregon State University (OSU). The numerical sub-assembly comprised the remainder of a three-span bridge, including models for the bridge abutments, shear keys at the tops of the piers, and springs representing soil-structure interaction (SSI) at the base of the piers. To simulate existing damage, seismic loading was applied offline in the structural numerical model before wave loading.

Given the significant variability of the tsunami wave breaking process, the advantage of this approach is that the fluid flow, wave-structure interaction, and potential hydro-elastic effects are modeled physically, their variability is explicitly represented, and additional sophistication is

gained from the coupled numerical sub-assembly, which can model the remaining bridge and realistic structural properties (mass, damping, geometric nonlinearities, and inelastic effects, e.g., from seismic loading). Yet despite its advantages, challenges exist for hydro-RTHS, including [i] the variable and high frequency pressure response that arises from the wave loading conditions, [ii] the execution of potentially large and computationally expensive numerical sub-assemblies in real or faster than real time, depending on similitude laws, and [iii] the robust control needed to mitigate experimental errors and stability concerns in a wet/submersible environment. To the author's knowledge, this is the first study of the cascading effects of earthquakes and tsunamis on bridge structures using RTHS with numerical seismic loading followed by physical wave loading.

Given that many coastal bridges in Oregon were constructed between the 1950s and the 1970s when both seismic and tsunami design loads were smaller than those currently considered, there is risk of severe damage to coastal bridges during such extreme events (Azadbakht and Yim 2016). Therefore, careful consideration and greater understanding of the impacts of tsunamis following seismic events is paramount to the assessment and design of coastal bridges. This study demonstrated the feasibility of using hydro-RTHS to enhance fluid-structure interaction simulations. Textbook short pulse response was exhibited by the specimen. Load cell information from the experiment and numerical model was used to validate the hydro-RTHS results. This illustrated that a real-time hybrid simulation approach is both feasible and economical for future investigations on this topic. Thus, hydro-RTHS virtually extends the capacity of the wave flume, enabling future holistic studies of wave-structure interaction with larger and more complex structures.

1.1. Research Objectives

The main objective of the work was to develop a real-time hybrid simulation approach to enhance wave-structure interaction simulations. To meet this objective, this study accomplished the following:

- Developed a hydro-RTHS architecture that simulates the wave-structure interaction physically and the remaining structure numerically.
- Demonstrated hydro-RTHS in a realistic testing environment to study the response of an idealized three-span bridge subjected to cascading seismic and tsunami events.

- Determined the extent to which hydro-RTHS enhances the simulation of wave-structure interaction by comparing forces from [i] wave loading on a fixed, unmoving specimen without hydro-RTHS, i.e., a *hold* boundary condition, [ii] wave loading on a moving specimen with a sinusoidal displacement response, and [iii] real-time hybrid simulation including seismic and hydrodynamic loading on a three-span bridge, i.e., hydro-RTHS.

1.2. Organization

This report is organized in four chapters. Following the introduction, Chapter 2 describes the materials and methods used to perform the hydro-RTHS experiments. The chapter includes a summary of the physical sub-assembly, numerical sub-assembly, and a discussion of the RTHS architecture and testing program. Chapter 3 discusses the experimental tests, including results for the pier specimen subjected to wave loading while held in a fixed position, wave loading while the specimen was displaced in a sinusoidal motion, and wave loading using hydro-RTHS with and without prior seismic damage. The latter used residual damage states from the earthquake loading as the initial state for the tsunami event simulated with hydro-RTHS. This chapter also includes an assessment of the results and preliminary validation of the hydro-RTHS method. Chapter 4 provides conclusions from the study, limitations, and suggestions for future work on this topic.

CHAPTER 2. MATERIALS AND METHODS

A three-span bridge model was partitioned at the top and bottom of a typical pier and divided into appropriate sub-assemblies for hydro-RTHS; see figure 2-1. The physical sub-assembly of this experiment comprised the tsunami waves and test specimen, which physically represented wave-structure interaction with a single bridge pier. The numerical sub-assembly comprised the remaining bridge structure, including a rotational spring representing SSI effects. First, the structure was numerically subjected to seismic loading, during which response history and residual damage were recorded. The damaged state was then used as the initial condition for the hydro-RTHS portion of the test, in which the tsunami loading was physically applied to the test specimen. Displacements enforcing compatibility between the sub-assemblies were applied in one degree-of-freedom by using a hydraulic actuator at the top of the pier. The measured force at the top of the pier, which implicitly included forces resulting from the wave actions, was then used to inform the state of the numerical sub-assembly (remaining three-span bridge, including SSI); see figure 2-1. The responses of the complete assembly (wave-bridge) and subsequent commands were obtained by executing a step-by-step numerical solution of the governing equations of motion given the coupled hybrid experimental-numerical system.
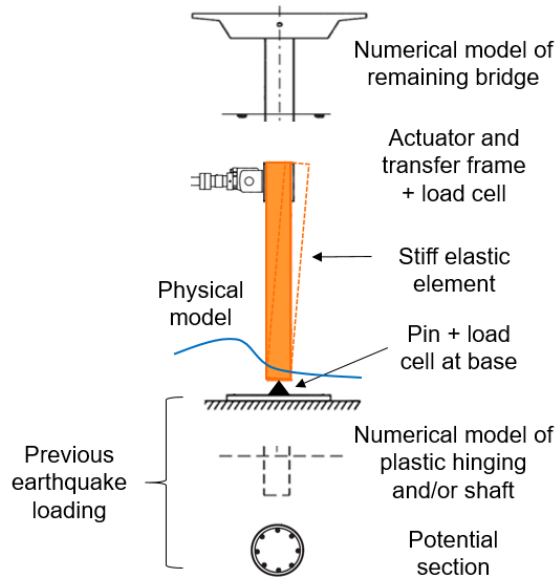
Figure 2-1. Physical-numerical partitioning of a three-span bridge.

2.1. Physical Sub-Assembly

This study was conducted at the Large Wave Flume (LWF) at the O.H. Hinsdale Wave Research Laboratory at OSU. The large wave flume was utilized to produce tsunami wave loading on the test specimen; see figure 2-2. The flume was 104.24 m long, 3.66 m wide, and 4.57 m deep. The maximum depth for solitary wave generation was 2 m, while the maximum depth for short (periodic) wave generation was 2.7 m. The LWF was equipped with a piston-type, dry-back wavemaker with a 4.2-m maximum stroke hydraulic actuator assembly, capable of generating short and long regular and random waves, as well as tsunami-type waves (solitary waves).

For this experiment, the bathymetry was configured with an impermeable 1:12 slope, 7.32 m long. The top of the horizontal section was 0.84 m from the flume bottom; hence, with a 2-m depth at the wavemaker, the horizontal testing section had a water depth of 1.16 m. The specimen was installed in the center of the flume's platform floor between bay markers six and seven.

8

(a)

(b)
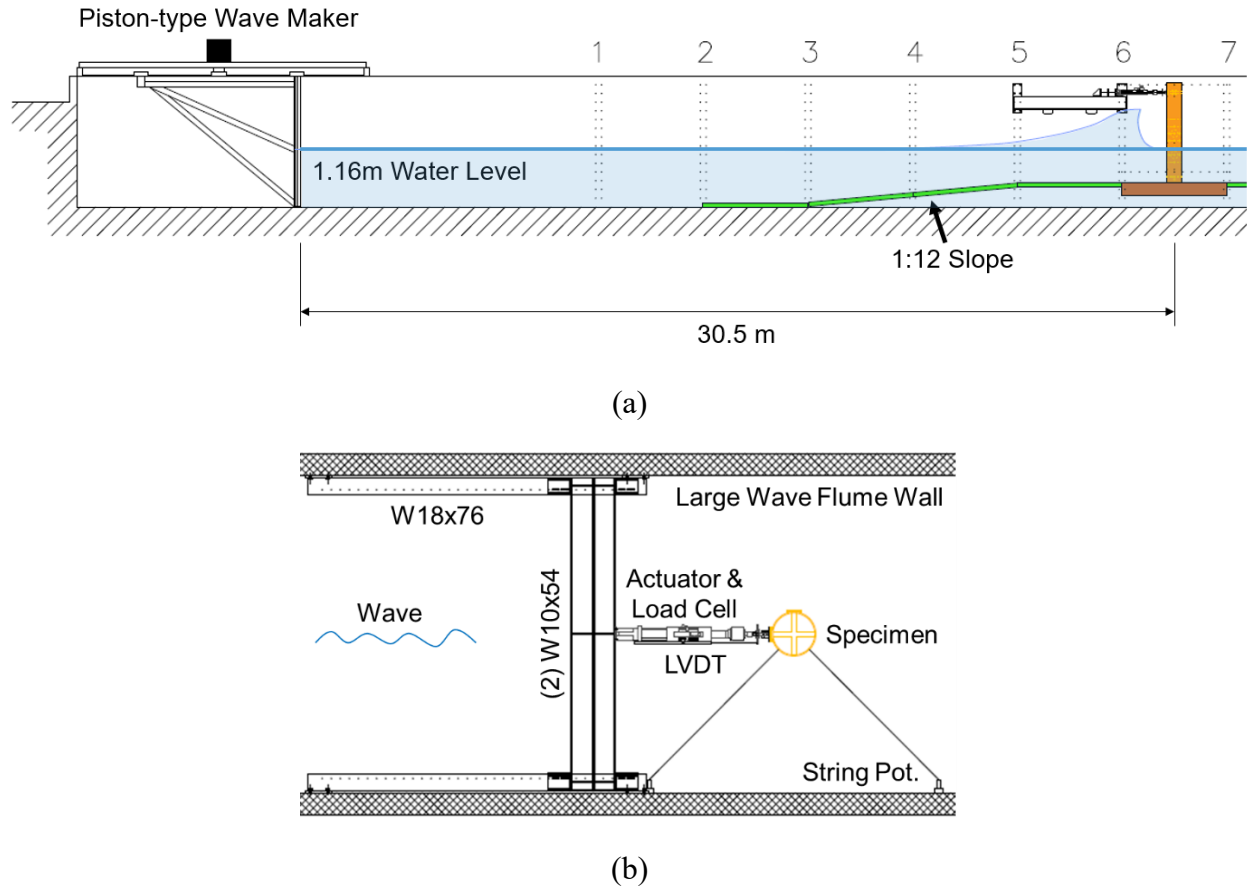
Figure 2-2. O.H. Hinsdale Large Wave Flume: (a) elevation, (b) plan.

2.1.1. Test Specimen

An existing hollow steel cylinder from a previous study (Lomonaco et al. 2019) was used as the test specimen for this experiment; see figure 2-3. Before this study took place, an orange powder coating was applied to prevent the steel from rusting; herein, the specimen will be referred to as the orange cylinder. At the base of the specimen, a clevis with a steel pin provided the attachment point to the wave flume floor. The base pin was installed such that the allowable degree of freedom for the cylinder was along the longitudinal axis of the wave flume, parallel to the wave loading. An additional clevis was installed at the top of the specimen on the loading face to provide the attachment point for a hydraulic actuator to displace the cylinder about the axis of the base pin.
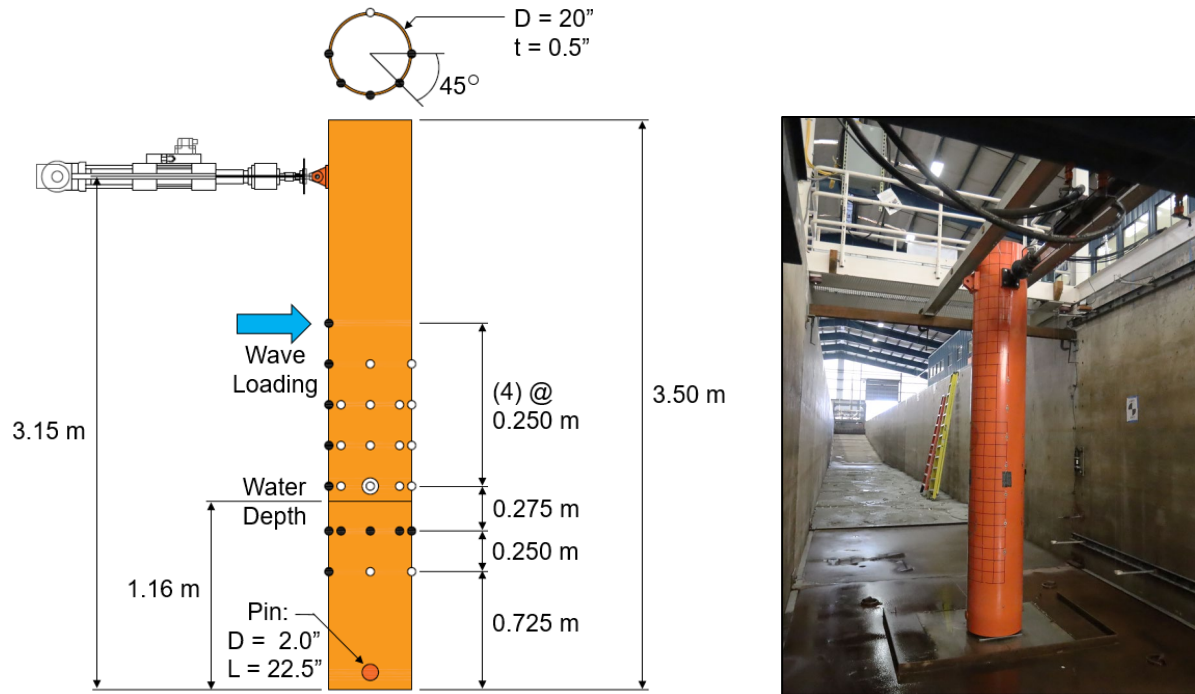
Figure 2-3. Test specimen.

2.1.2. *Test Setup*

The experimental setup was designed to actuate residual displacements representing previous seismic loading and displacements from subsequent wave loading at the top of the pier.

A transfer frame was installed along the walls of the wave flume; see figure 2-4. Two W18x76 steel girders were bolted to the wave flume walls along its longitudinal direction. Two additional W10x54 steel beams were first bolted together along one flange and then attached to the top of either transfer girder to span the width of the wave flume. In the center of the beam span, mounting holes were drilled into the flange to facilitate connection of the clevis attaching to the actuator.

To limit out-of-plane displacement of the specimen during testing, two aluminum guide rails were installed on either side of the test specimen at a height approximately parallel to that of the hydraulic actuator. These were held in position using pipe clamps; see figure 2-4.

10
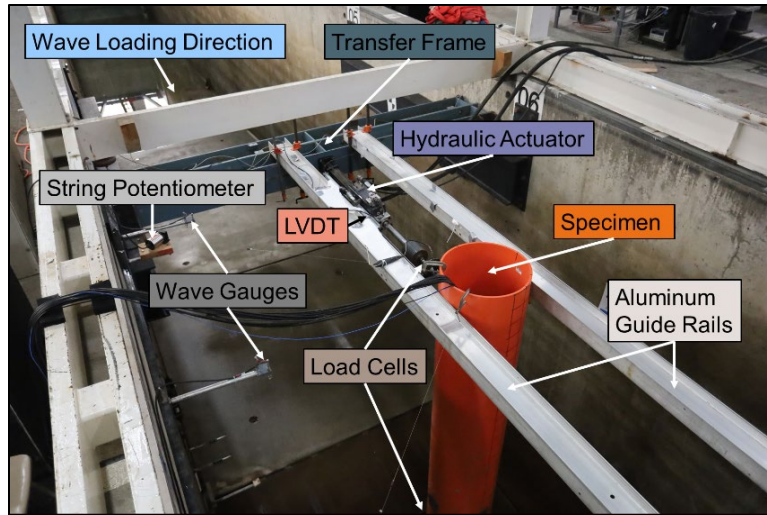
Figure 2-4. Physical sub-assembly test setup.

2.1.3. *Actuation*

A hydraulic MTS actuator was used to apply displacements to the top of the specimen; see figure 2-5. This actuator had a capacity of 4.5 kips and 12 inches of dynamic stroke. The clevis end of the actuator was bolted to the beam of the transfer frame, while the rod end of the actuator was bolted to the top of the test specimen by use of a fabricated clevis. The clevis at the top of the specimen was oriented such that lateral displacements causing rotation about the pin at the bottom of the specimen were not impeded. The actuator was connected to one of the laboratory MTS hydraulic service manifolds with hydraulic hoses.

An external linear variable displacement transducer (LVDT) was attached to the actuator to measure displacement at the top of the test specimen. The body of the LVDT was clamped to the side of the MTS actuator, and the rod end of the LVDT was attached to a circular plate mounted to the rod end of the actuator. A MOOG servo-valve with a capacity of 16.5 gallons per minute (GPM) was used in conjunction with the actuator for testing.

Figure 2-5. The MTS hydraulic actuator.

2.1.4. Instrumentation

Instrumentation included a hydraulic actuator with an external LVDT, string potentiometers, wave gauges, and load cells (see figure 2-4).

1.1.1.1 Load Cells

Two load cells were used to collect loading data during the experimental tests: one at the base of the specimen and one at the top of the specimen. The load cell at the top of the test specimen was an in-line model and had a capacity of 10 kips. It was used to measure the force feedback in the direction of loading, along the longitudinal direction of the wave flume, which was inputted into the equations of motion for RTHS. The load cell was installed parallel to the hydraulic actuator, placed in-line between the rod end and the fabricated clevis.

The load cell at the bottom of the test specimen was bolted between the clevis at the base of the specimen and the floor of the wave flume. It had six degrees of freedom and a capacity of 7.2 kN in the transverse and longitudinal directions of the flume, 18 kN in the vertical direction, and 1400 N-m in all directions of rotation. This load cell was used to measure forces along, and about, all three principal axes during the tests. This load cell was used to monitor the specimen forces only and was not used as feedback within the RTHS setup, because the numerical model did not have degrees of freedom at this location. The base load cell was associated with reactions at the base boundary condition and not the degrees of freedom used in the equations of motion of the numerical model.

1.1.1.2 Pressure Sensors

Various hole locations for the installation of pressure sensors were available on the specimen's circumference, and 11 holes were populated to measure wave loading data for this study (see figure 2-3). Seven were installed along the loading face of the specimen. The remaining four sensors wrapped around one side of the cylinder at a height just below the water depth in the flume.

1.1.1.3 String Potentiometers

Two string potentiometers were used to measure displacements and velocities during the tests. They were both attached to the wave flume walls, with targets at the top of the test specimen. The first potentiometer was mounted next to bay marker 6 of the wave flume wall and was attached to the specimen at an angle of 45° counterclockwise from the loading face of the specimen. The second potentiometer was mounted next to bay marker 7 of the wave flume wall and was attached to the specimen at an angle of 135° degrees counterclockwise from the loading face of the specimen.

1.1.1.4 Wave Gauges

Three sets of wave gauges were used to measure the wave heights during the tests. The first gauge was attached to the wave flume wall next to bay marker 6; the second gauge was attached to the wave flume wall halfway between bay markers 6 and 7; and the third gauge was attached to the wave flume wall next to bay marker 7.

2.2. Numerical Sub-Assembly

The numerical sub-assembly representing the remainder of the three-span bridge was modeled in the open-source, finite-element analysis framework OpenSees (McKenna et al. 2010) to simulate the response of the remaining bridge and previous damage due to seismic loading; see figure 2-6.
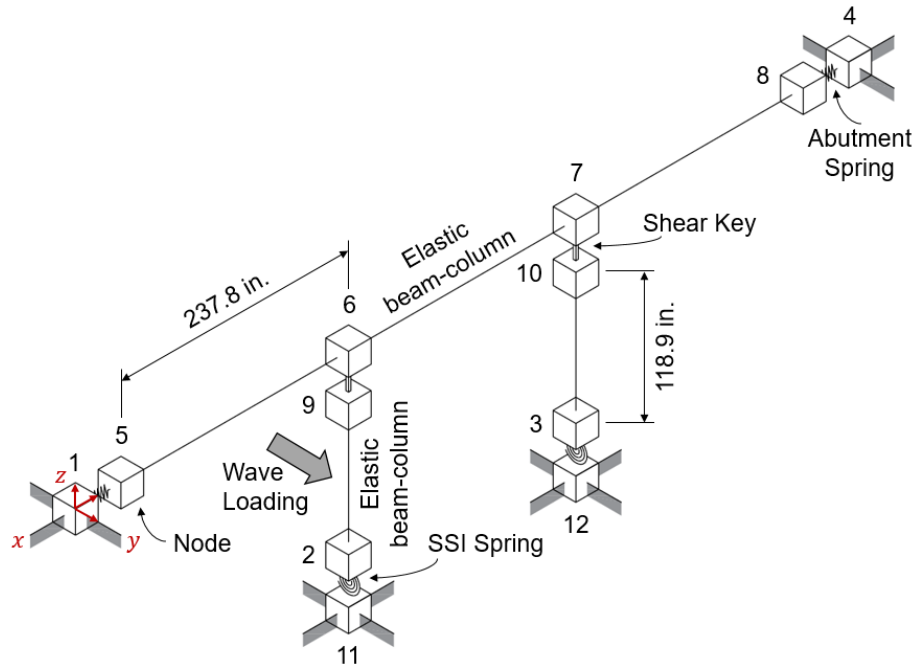
Figure 2-6. Numerical bridge model.

2.2.1. Reference Five-Span Bridge Model

An existing reference bridge model from a parallel study was used in designing the bridge model for the hydro-RTHS tests. The reference bridge was developed according to AASHTO (AASHTO 1996) and California Transit (Caltrans) Seismic Design Criteria (SDC) (Caltrans 2004). The model included various options for abutments, piers, decking, and foundations. The moment-rotation properties of the SSI spring were based on the expected behavior of a single pile with a soil profile of 15 feet of soft plastic silt over sandstone.

Although the reference bridge model had been used extensively by many researchers to study bridge response to seismic loading (Ketchum et al. 2004, Traubita 2009, Aviram et al. 2012), as the first application of hydro-RTHS for tsunami loading, the bridge model was intentionally simplified to alleviate sources of error and to ensure that testing could be conducted in real time.

2.2.2. Bridge Model Scaling

An existing, highly idealized "dummy" bridge model, used previously to troubleshoot geographically distributed hybrid simulation for seismic loading (Schellenberg et al. 2009), was scaled to the geometry of the existing cylinder specimen to achieve roughly realistic structural

periods. Material properties from the reference five-span bridge model were then scaled down and simplified for this new dummy model. In this fashion, there were no similitude differences between the physical and numerical sub-assemblies, and material properties were highly idealized and simplified; future work can then build upon this study to implement the similitude advantages gained by using hydro-RTHS.

To scale the material properties from the reference model, dynamic similitude for wave-structure interaction encompassed equilibrium between several forces:

$$F_i + F_\mu + F_g + F_e + F_p + F_s \ldots = 0 \qquad \text{Eq. 1}$$

where: F_i = inertial forces, F_μ = viscous forces, F_g = gravitational forces, F_e = elastic forces, F_p = pressure forces, F_s = surface forces. Unless the experiment was at full scale, perfect dynamic similitude between all forces in a small-scale physical system would be impossible. Froude scaling uses the relationship of inertial forces to gravitational forces and is typically prioritized when the dynamics of the fluid are most important to a study. Cauchy scaling uses the relationship of inertial forces to elastic forces and is typically prioritized when the dynamics of the structure are most important to a study.

The section dimensions and properties of the piers were defined by considering the section properties of a solid cylindrical bridge pier with a diameter of 20", the same diameter as the hollow steel orange cylinder. On the basis of the existing cylinder height, Cauchy scaling with a scale factor of $\lambda_L = 2.20$ was used to scale up the dimensions of the dummy three-span model to the height of the existing orange cylinder specimen, including material properties for the abutments. Additionally, Cauchy scaling was used to scale down the material properties of the deck, mass, and gravity loading of the reference five-span bridge model based on the spans of the new, scaled-up three-span dummy model with a scale factor of $\lambda_L = 7.6$. The SSI springs were scaled down by $\lambda_L = 2.22$ based on the height of the piers of the five-span bridge relative to the height of the cylinder. This resulted in a relatively low-stiffness rotational spring at the base of each pier. By Cauchy scaling, all force metrics were scaled by λ_L^2 (Froude scaling uses λ_L^3).

The material properties defined in the model were also reduced to represent cracked, reinforced concrete from the reference bridge; see table 2-1. These properties were highly idealized but resulted in periods suitable to observe structural dynamic excitation for both the seismic and tsunami loading. The more realistic five-span model will be tested in a subsequent

15

study, including parallel computing (see Appendix B) and partitioned scaling laws across the numerical and physical sub-assemblies.

Table 2-1. Deck and pier element material properties.

Element	Area, A	Young's Modulus, E	Shear Modulus, G	Torsional Moment of Inertia, J	Second Moment of Inertia, I_y	Second Moment of Inertia, I_z
Deck	999 cm^2 (154.8 in^2)	27600 MPa (4002.0 ksi)	11500 MPa (1667.0 ksi)	46000 cm^4 (4420×0.25 in^4)	42300 cm^4 (2060×0.5 in^4)	820000 cm^4 (39420×0.5 in^4)
Pier	2030 cm^2 (314.16 in^2)	27600 MPa (4002.0 ksi)	11500 MPa (1667.0 ksi)	163000 cm^4 (15708×0.25 in^4)	163000 cm^4 (7854×0.5 in^4)	163000 cm^4 (7854×0.5 in^4)

2.2.3. *Three-Span Bridge Model*

The scaled three-span bridge model was three-dimensional (see figure 2-6). Twelve nodes were used to model the bridge geometry: two at each abutment, two at the top of each pier, and two and the bottom of each pier. Nodes one, four, eleven, and twelve were fixed in all translational and rotational directions. Nodes two and three were fixed in all translational directions but fixed in torsion only about the global z-axis. The mass of the bridge was assigned and distributed along the nodes that composed the bridge deck (nodes six and seven) and the bridge abutments (nodes five and eight). $P\Delta$ geometric transformations were used for the bridge pier and deck elements. Stiffness-proportional Raleigh damping of 3 percent based on the initial stiffness was assigned to a period of 1.0 sec, similar to the period in the transverse direction of the bridge.

The bridge piers and deck spans were modeled with elastic beam-column elements. This element type was chosen because the members of the bridge would experience both axial forces from overturning moment and gravity loading, as well as flexure from the seismic excitation and tsunami loading.

To model potential soil-structure interaction at the base of the pier, the two nodes at the bottom of each pier were connected by using a zero-length element to represent rotational deformations due to the seismic and wave loading; see table 2-2. The two sets of nodes at the top of each pier were linked by using zero-length elements to define shear keys with very stiff elastic properties in all translational directions. These shear keys were used to model resistance against the applied lateral seismic and tsunami loading and sliding forces.

To model the abutments, nodes five and eight were linked to one and four, respectively, by using elastomeric bearing plasticity elements, which have coupled plasticity properties for shear deformations. The remaining force-deformation behavior in the remaining four directions of the abutment was defined by the material properties with a linear post-yield slope; see table 2-2. Material properties for the axial, torsional, and moment directions of the abutment were modeled with an elastic material with large stiffness.

Table 2-2. SSI spring and abutment material properties.

Element	Yield Strength	Initial Stiffness	Strain Hardening Ratio
SSI Spring	153 kN-m (1356 kip-in.)	1030 kN-m (9141 kip-in.)	0.3
Abutment	129 kN (29.1 kips)	4620 kN/m (26.4 kip/in.)	0.05

2.2.4. Sub-Assembly Partitioning

The degrees-of-freedom along the longitudinal direction of the flume used for the command displacement and measured force feedback were co-located at the top of the test specimen, which corresponded to the top of the bridge pier in the numerical sub-assembly. To satisfy equilibrium with the load cell at the base of the physical cylinder and the reaction at the base of the numerical sub-assembly, including the SSI spring, a very stiff elastic beam-column element was used to emulate a rigid link between degrees-of-freedom two and nine, essentially condensing out degrees of freedom associated with the pin in the physical sub-assembly; see figure 2-7.
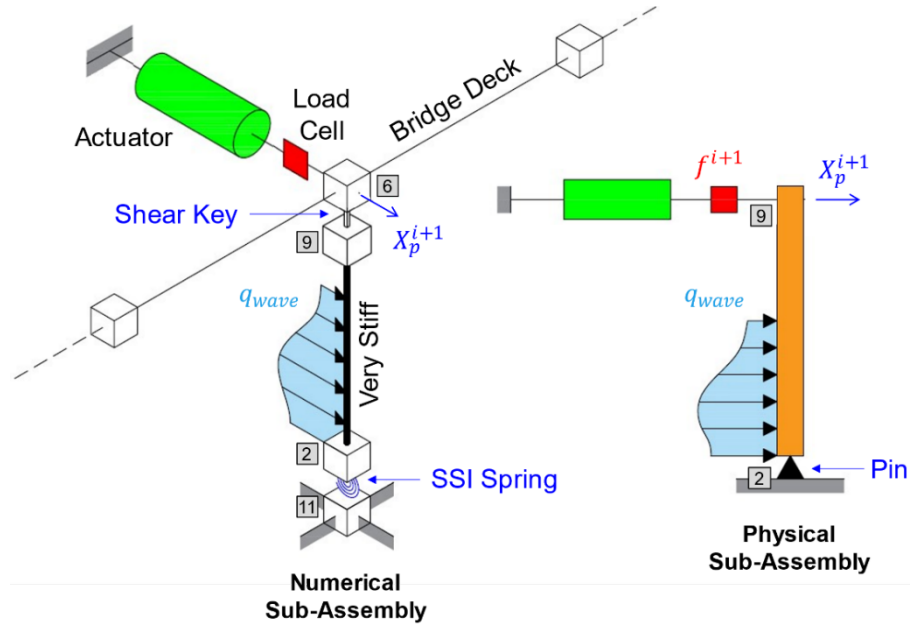
Figure 2-7. Numerical and physical sub-assemblies.

2.2.5. *Eigenvalue Analysis*

An eigenvalue analysis of the three-span bridge was performed after gravity loading had been applied; see table 2-3. Mode 1 corresponded to the transverse bridge direction, and mode 2 corresponded to the longitudinal bridge direction.

Table 2-3. Three-span bridge eigenvalue analysis.

Mode, n	Circular Frequency, ω_n [rad/sec]	Period, T_n [s]	Frequency, f_n [Hz]
1	5.44	1.16	0.87
2	11.46	0.55	1.82
3	15.78	0.40	2.51
4	28.16	0.22	4.48
5	28.72	0.22	4.57
6	192.26	0.03	30.60

2.3. Real-Time Hybrid Simulation

In real-time hybrid simulation, the test is executed with the same time scaling needed to satisfy dynamic similitude (herein, the orange cylinder is considered to be "full-scale" and the

time scale is real time). Thus, RTHS allows investigation of structural systems with rate-dependent components, like the real-time flow of the water used in this study. A suite of system numberers, integrators, and algorithm variations were tested to determine analysis parameters for the fastest computations within the desired time step of 10/2048 (10 times slower than the sampling of the controller), while still being comparable to results from the reference five-span model; see Appendix A. Generalized-alpha-OS was chosen, as it provided the fastest computation time as well as the largest range of possible numerical damping inputs.

2.3.1. Equations of Motion

The system response to an external excitation at the next time step can be modeled by using the equation of motion, discretized in time; see figure 2-8:

$$M\ddot{X}^{i+1} + C\dot{X}^{i+1} + R_n^{i+1} + f^{i+1} = F^{i+1} \qquad \text{Eq. 2}$$

where i = integer representing the time step, M = mass matrix, C = damping matrix, $X: X_p; X_n$ = vector of displacements applied via actuation in the physical sub-assembly and applied virtually in the numerical sub-assembly, respectively; R_n^{i+1} = restoring forces calculated in the numerical sub-assembly, f^{i+1} = restoring forces measured from the physical sub-assembly, and F^{i+1} = applied seismic loading.
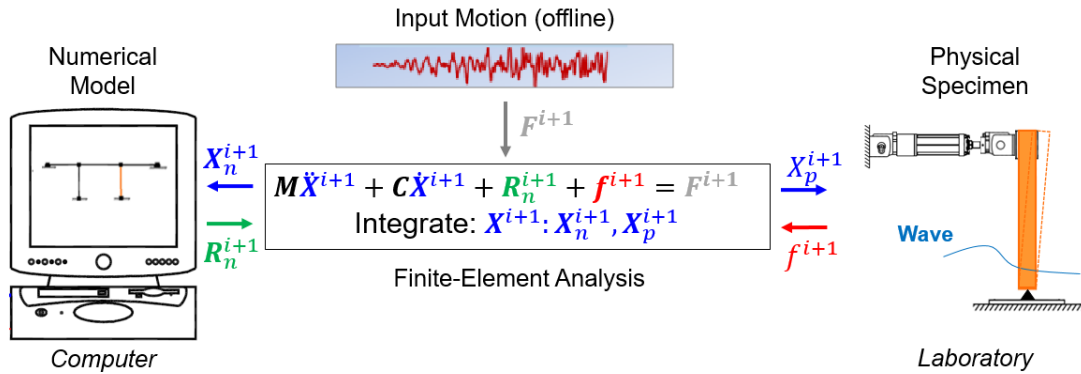
Figure 2-8. Hydro-RTHS schematic for seismic and hydrodynamic loading

The partitioning was selected such that the wave loading and hydrodynamic pressures were indirectly measured through the load cell located at the top of the cylinder (see figure 2-5). This measurement was then used as an applied load input into the right-hand side of the equation of motion:

$$M\ddot{X}^{i+1} + C\dot{X}^{i+1} + R_n^{i+1} = -f^{i+1} \qquad \text{Eq. 3}$$

19

where f^{i+1} = interface force feedback measured from the load cell at the top of the displaced specimen to the wave loading acting on the cylinder. Thus, the equation of motion could be written in terms of only the structural dynamics without the need for equations representing the fluid dynamics and the wave-structure interaction effects.

Initially, seismic loading was applied to the three-span bridge in a purely virtual manner to obtain initial damage states. For the subsequent hydro-RTHS, the displacements were known at the beginning of a time step, X^{i+1}. The displacements of the physical, X_p^{i+1}, and numerical X_n^{i+1}, sub-assemblies were extracted from X^{i+1}. Force feedback, f^{i+1}, was measured by using the load cell at the top of the cylinder specimen displaced to X_p^{i+1} and the wave loading acting on the structure, q_{wave}. Restoring forces in the numerical sub-assembly, R_n^{i+1}, were computed by using the finite-element model of the remaining bridge model with the numerical sub-assembly displacements, X_n^{i+1}, and interface forces, f^{i+1}, including the SSI springs at the base of the piers. These forces were used as inputs to the equations of motion in Eq. 3. Using the numerical analysis within OpenSees, the resulting displacements for the following time step, X^{i+2}, was calculated by integrating the equation of motion for displacement. The process was then repeated for all remaining time steps of the test.

2.3.2. Integration Method

While the implicit Newmark method (Newmark 1959) is a popular choice for numerical integration in the field of structural engineering, it is not suitable for RTHS because the method is iterative and may not converge during real-time testing. Instead, specialized integration schemes are needed for RTHS, e.g., explicit (Kolay and Ricles 2014) or fixed iteration (Dorka and Heiland 1991, Zhong 2005) time-stepping schemes with unconditional stability and numerical damping to suppress higher-mode excitations due to experimental errors (Schellenberg et al. 2009).

For example, semi-implicit operator-splitting (OS) integration schemes (Hughes et al. 1979, Hulbert and Chung 1996) satisfy the RTHS criteria (Schellenberg et al. 2009). The OS algorithm is a predictor-one corrector scheme that does not require iterations and can achieve unconditional stability for nonlinear stiffness softening-type structural behavior if re-formulated for RTHS [alpha-OS (Nakashima et al. 1990, Wu et al. 2006, Schellenberg et al. 2009) and generalized-alpha-OS (Schellenberg et al. 2009)].

The physical and numerical sub-assemblies were coupled by using the equation of motion and the generalized-alpha-OS numerical integration method with $\rho_\infty = 0.5$, which defined the amount of numerical damping. With a $\rho_\infty = 0.5$, the generalized-alpha method was equivalent to the alpha-OS method by using $\alpha = 2/3$. This ρ_∞ resulted in a moderate amount of numerical damping permissible for the method and was used here to suppress experimental errors for this pilot study. These errors stemmed from undamped higher-mode vibrations from the real experimental setup that could propagate and render the simulation unstable.

2.3.3. Three-Tier Architecture

To increase flexibility, the three-tier architecture framework for RTHS developed by Mosqueda (2003) was used in this study; see figure 2-9. The three loops of the system included [1] a simulation *host* computer housing the finite-element analysis software, OpenSees, [2] a real-time *target* computer, and [3] a *controller* and data acquisition system. These three hybrid simulation nodes were connected by using a shared common random access memory network (SCRAMNet+) and fiber optic cables to facilitate near-instantaneous communication across the machines. Provided that the numerical analyses could execute a time step fast enough because of small-scale similitude requirements, these connections could make it possible to execute simulations in real time.
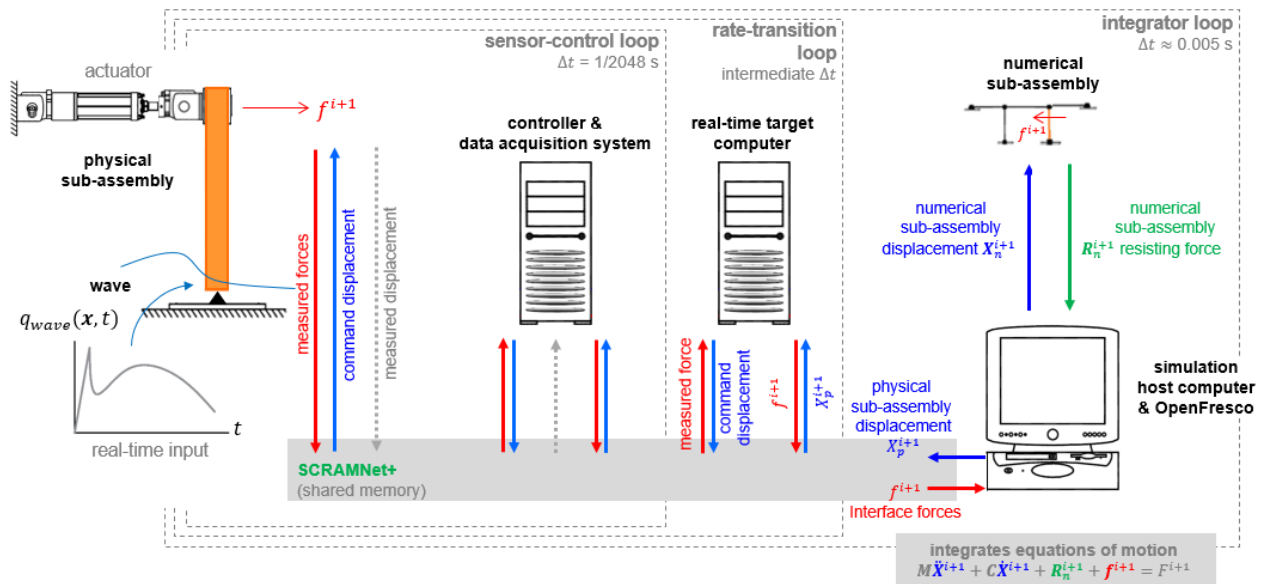

Figure 2-9. Three-tier architecture

Since processes on each machine are explicitly separated, the three-tier architecture gives the hydro-RTHS framework the flexibility to use any finite-element or driver software on the

21

simulation host computer without the need to modify that software to run in real time. The finite element model for the numerical sub-assembly resides in the simulation host computer. OpenFresco, also housed in the simulation host computer, is an existing open-source software platform used to set up and coordinate integration between the physical and numerical sub-assemblies in hybrid simulation (Schellenberg et al. 2009). The OpenFresco middleware supports a large variety of computational drivers, structural testing methods, platform types, testing configurations, control and data acquisition systems, and communication protocols.

The controller and data-acquisition (DAQ) system controls and monitors the motion of the physical-assembly induced by the actuation and physical wave actions. In between the host and controller, the real-time target computer facilitates time synchronization between the host computer (which completes a time step of $\Delta t \approx 0.005$ sec) and controller (which runs in real time, $\Delta t = 1/2048$ sec). This intermediate machine generates commands in real time from the finite-element software that are sent to the controller. Algorithms that enable real-time testing, including delay compensation (Chae et al. 2013) and predictor-corrector algorithms (Schellenberg et al. 2009) between the finite element software and the controller, reside on the target computer.

2.3.4. Simulink Model

The Simulink model on the target machine handles the tasks needed for RTHS; see figure 2-10. Simulink is a programming software used for modeling, simulating, and analyzing multi-domain dynamic systems. The Simulink model housed [i] an adaptive time series (ATS) compensator (Chae et al. 2013) to mitigate time delays between the command and feedback signals and [ii] a predictor-corrector algorithm to facilitate smooth displacement history of the test specimen during the experiment. The Simulink model was run on the target machine within the Simulink real-time operating system. OpenFresco (Schellenberg et al. 2009) was used as the communication bridge between OpenSees on the host machine and the Simulink model on the target machine.

Figure 2-10 shows the Simulink model that was used in this real-time hybrid simulation test. The left-hand side of the figure shows the input blocks for both OpenFresco and the MTS controller. Forces and the displacements for each time step were extracted from both the numerical model and the load cells from the physical specimen. The displacement values from the specimen were sent to a delay compensator, which used a recursive least squares solver to

mitigate mismatch in time between the displacement signal sent from the controller and the measured displacement of the specimen (Chae et al. 2013).
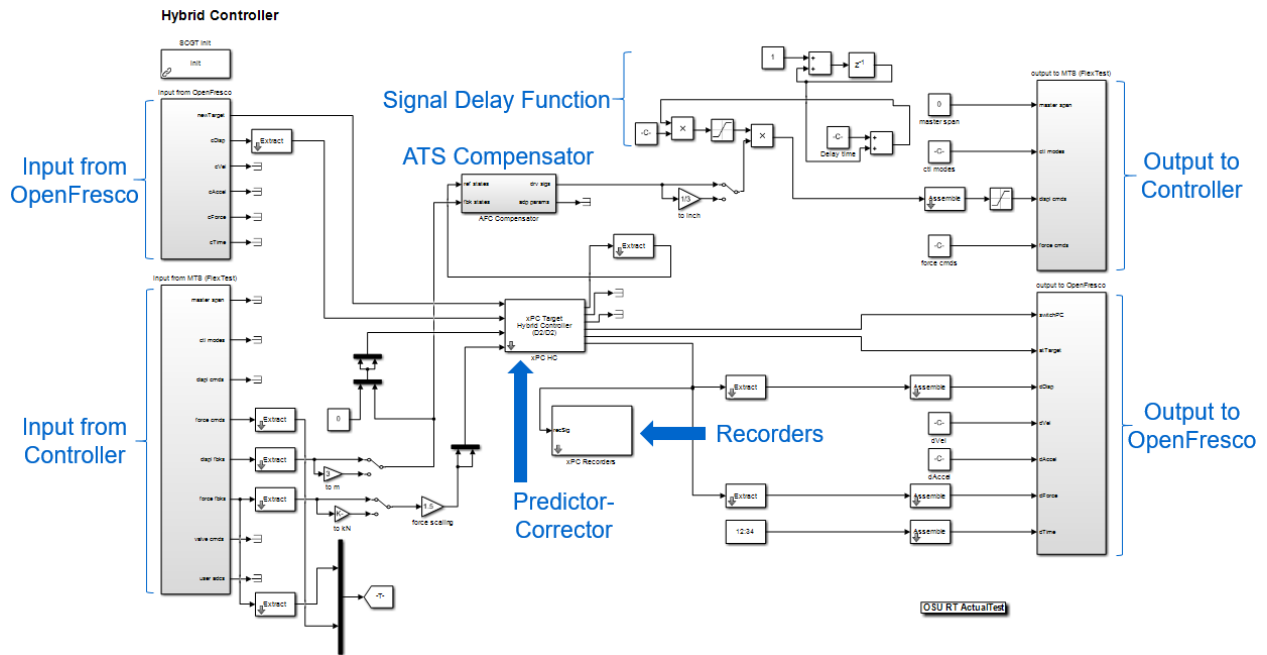
Figure 2-10. Simulink **r**eal-**t**ime **m**odel

The loop shown in the upper right of the Simulink model contains a controller signal delay function. Since the displacements from the seismic loading were expected to exceed the stroke of the actuator, the time-delay function was implemented to ensure that physically applied displacements did not exceed the limitations of the hydraulic actuator during the seismic loading of the test; i.e., seismic loading was only applied virtually. The function inhibited sending of the displacement command signal to the actuator for the duration of the earthquake. After the counter ended, the command signal was then ramped up to its full value over a 5-second interval to apply any residual displacement from the seismic loading in preparation for the tsunami loading. The full displacement signal for the response of the structure was then permitted to be sent to the specimen for the subsequent tsunami loading. By executing tests in this offline manner, the numerical model experienced the full seismic event and damage, and residual displacements were safely applied to the physical specimen.

1.1.1.5 Adaptive Time Series (ATS) Compensator

A compensation scheme, termed the adaptive time series (ATS) compensator (Chae et al. 2013), was used to mitigate time delays between the actuator command and feedback signal; see figure 2-11. Lagging feedback can result in negative damping and instabilities when the equation of motion is integrated. The ATS compensator reduces variable time delays that could arise because of the actuator dynamics and signal delays and/or nonlinearity of the experimental specimen. With the ATS compensator, system transfer function coefficients are updated in real time using linear regression analysis to avoid user-defined adaptive gains, which are typically calibrated only on the basis of a trial-and-error process. In eliminating calibration setup and accounting for nonlinear response during testing, the ATS compensator improves accuracy in actuator control and reduces the chance of accidental damage to the specimen.
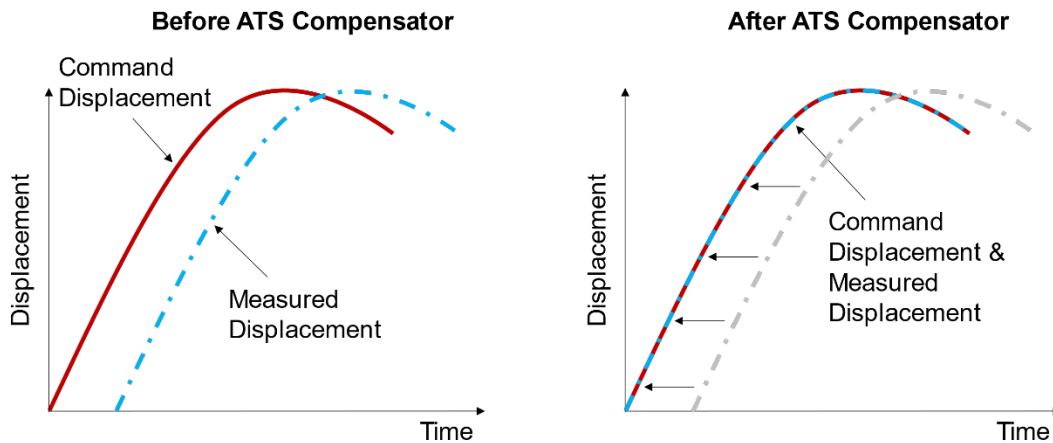
Figure 2-11. Displacements before and after the ATS compensator.

1.1.1.6 Predictor-Corrector

A deterministic control scheme could fail if the finite-element analysis does not deliver output at the allotted time. A predictor-corrector algorithm (Mosqueda 2003, Schellenberg et al. 2009) was used to synchronize commands between the finite-element analysis and the servo-hydraulic control system to provide a smooth transition between the controller, which is deterministic with a sampling rate of 2048 Hz, and the finite-element analysis residing on the host machine, which could have a variable solution time for each time step.

While the finite-element analysis was solving the equations of motion for the displacement commands at the next time step, a polynomial curve, defined by $x \in [0,1.0]$, was

used to extrapolate (predict) commands into the future and interpolate (correct) commands upon receiving the results from the finite-element simulation (Nakashima and Masaoka 1999); see figure 2-12. The last point of prediction, as well as the last two known points of displacement and trial velocities, were used to determine the new calculated displacement for the specimen, which were sent to the controller at a deterministic rate. The open circles in the figure represent the controller time step of 1/2048 seconds, while the filled circles represent the integration/ simulation time steps. If 60 percent of the simulation time step was reached before a displacement had been calculated, the predictor slowed the command signals in an effort to prevent jerks in the actuator motion. If 80 percent of the simulation time was reached before a displacement had been calculated, $x_p \in [0,0.8]$, the predictor completely stopped the command signal. Afterward, the signal to the actuator steadily increased back to full until 100 percent of the time step had occurred. At the end of each time step, the displacement signal was sent back out to both the MTS controller and OpenFresco. This process was repeated for each time step during the hydro-RTHS test until completion.
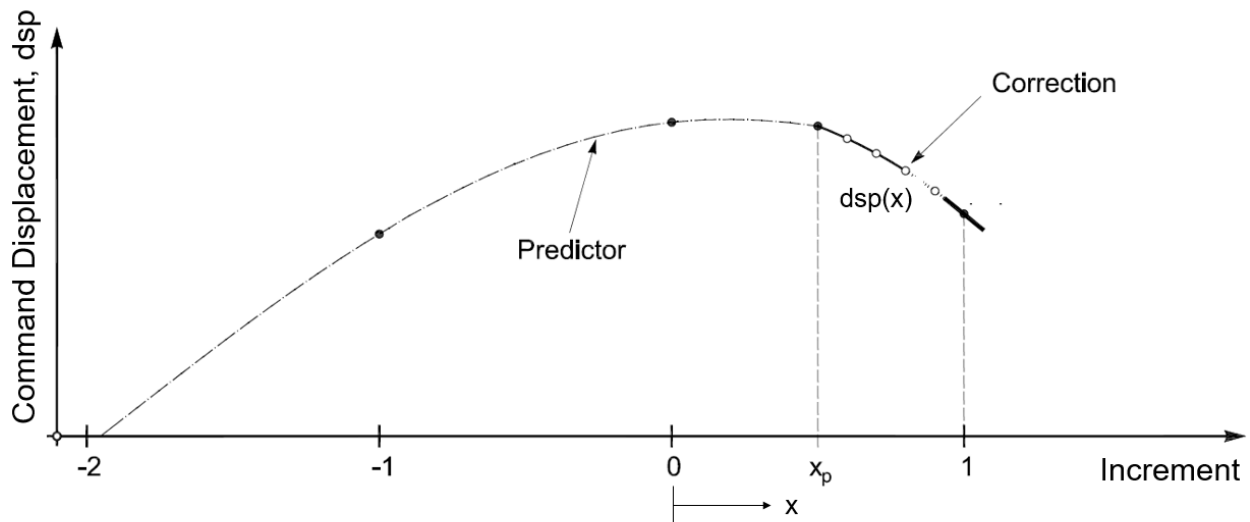
Figure 2-12. Predictor-corrector (Schellenberg et al. 2009).

2.4. Testing Program

The testing matrix for promising test runs are shown in table 2-4. For initial trials, the specimen was held by the hydraulic actuator during the tsunami loading, representing a near-rigid baseline, or *hold*, case. For the second set of trials, a sinusoidal displacement command was

used to move the specimen to represent potential structural vibrations during the hydrodynamic loading, the *sine* case. For the third set of trials, the tsunami wave was applied without the initial seismic loading in a pure hydro-RTHS setting. In the final phase of trials, seismic loading was applied virtually to the numerical model of the three-span bridge; then, physical waves were applied to the specimen via hydro-RTHS.

Table 2-4. Testing matrix.

Trial	Test	Event	Station	RSN	Seismic Scale Factor	Wave Scale Factor	Water Level [m]	Wave Type	Wave Height [m]	Bridge Piers Impacted	Time delay [msec]	Maximum RMS Error [%]
16	Hold	-	-	-	-	1.0	1.16	Solitary	1.4	-	-	-
17	Hold	-	-	-	-	1.0	1.16	Solitary	1.4	-	-	-
18	Sine	1 Hz	-	-	-	1.0	1.16	Solitary	1.4	-	-	-
19	Sine	1 Hz	-	-	-	1.0	1.16	Solitary	1.4	-	-	-
20	Sine	1 Hz	-	-	-	1.0	1.16	Solitary	1.4	-	-	-
21	Sine	1 Hz	-	-	-	1.0	1.16	Solitary	1.4	-	-	-
22	Sine	2 Hz	-	-	-	1.0	1.16	Solitary	1.4	-	-	-
03	hydro-RTHS only	-	-	-	-	1.0	1.16	Solitary	1.4	1	-4	0.275
06	hydro-RTHS with seismic loading	Superstition Hills	El Centro	721	2.0	1.5	1.16	Solitary	1.4	1	0	0.216
08		Kobe	JMA	1106	1.5	1.5	1.16	Solitary	1.4	1	0	0.052
09		Kobe	Takatori	1120	1.0	1.5	1.16	Solitary	1.4	1	-2	0.103
10		Tohoku	MYG015	4001066	1.0	1.5	1.16	Solitary	1.4	1	0	0.236
19		Superstition Hills	El Centro	721	2.0	1.5	1.16	Solitary	1.4	2	0	0.081

Before the tsunami loading phase of the experiment, the numerical model was subjected to a suite of representative ground motions applied uniformly at the base of the bridge structure in the lateral, transverse, and vertical directions. On the basis of previous studies using the five-span reference bridge (Traubita 2009), the B-ICC El Centro record from the large moment-small distance (LMSR) ground motion bin (Krawinkler et al. 2003) was defined with a scale factor of 2.0, resulting in a combined peak ground velocity (PGV) of 123.56 cm/sec (48.65 in/sec) and representative of a relatively high intensity ground motion. Based on studies of several existing ground motion databases [e.g., (Baker et al. 2011)], the unscaled Takatori and JMA Kobe ground motion records were added as they each resulted in large and damaging bridge displacements.

Additionally, the Tohoku earthquake was selected from the NGA-Sub database (Bozorgnia 2020) as representative of a recorded cascading earthquake and tsunami event (Carey et al. 2019).

A single, solitary tsunami-like wave type was applied to the specimen for all experimental tests. This wave type produced the largest forces induced in the test specimen because of the cylinder's location along the wave flume. More extreme impact could have been observed had the cylinder been placed farther along the wave flume (Lomonaco et al. 2019). Use of a single wave type also allowed for the representation of potential variability in the wave loading over consecutive test runs.

Force feedback for the hydro-RTHS tests was scaled from 1.0 to 1.5 for the tsunami events to emulate the higher density of real tsunami waves due to salt water and the accumulation of debris and particulates. This could not be physically simulated in the wave flume, which out of necessity used regular water. This effect could not be studied with clear water without hydro-RTHS.

As a pilot study, wave loading was initially applied to only one bridge pier in the hydro-RTHS tests. To better represent the effects of a tsunami wave on multiple bridge piers, during the final test run, the force feedback from the load cell in the physical sub-assembly was copied and applied to both bridge piers before the equations of motion were integrated to solve for the next time step.

CHAPTER 3. RESULTS AND DISCUSSION

The results of the various tsunami loadings on the modeled bridge are presented in terms of the hold and sine wave loading and the hydro-RTHS trials.

3.1. Hold Wave Loading

An initial set of trials was performed as a baseline case. Solitary waves were applied to the cylinder while the actuator was held steady with the hydraulics turned on; i.e., displacements at the top of the cylinder were essentially zero. The waves initially began at a height of 0.5 meters and were gradually increased until the maximum force at the load cell at the top of the cylinder was observed, which was determined to be at a height of 1.4 meters. As shown in figure 3-1, the force at the load cell was relatively consistent between runs of the same wave case (see sign convention in figure 3-2); 4.00 kN for Trial 16 and 3.92 kN for Trial 17. This maximum reaction corresponded to the instance in which the wave broke at the position of the specimen, rather than before or after its location.

Top of Cylinder Top of Cylinder Bottom of Cylinder

(a)

(b)
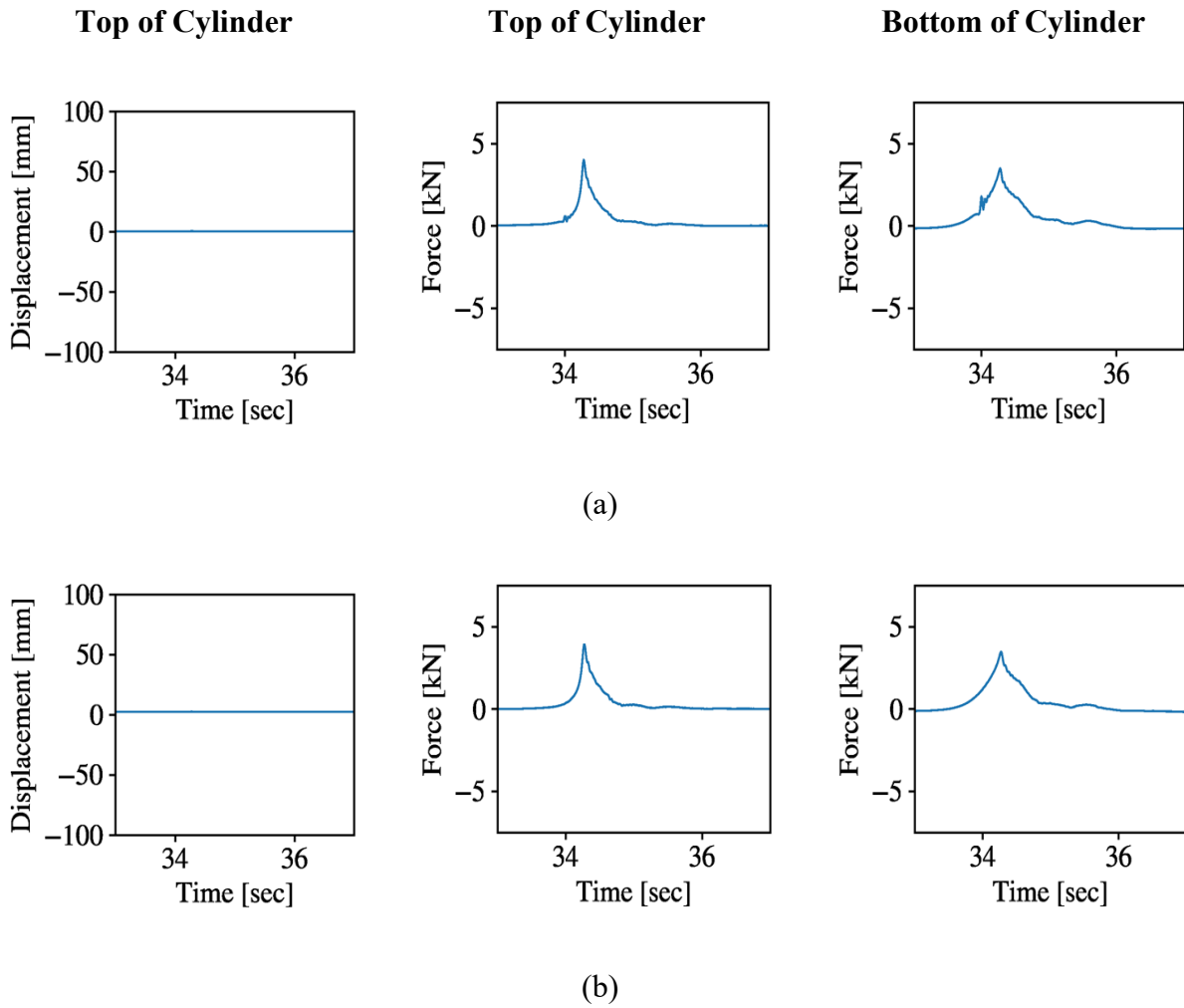
Figure 3-1. Displacement at top of cylinder, force at top of cylinder, and force at bottom of cylinder for hold wave loading: (a) Trial 16, (b) Trial 17.
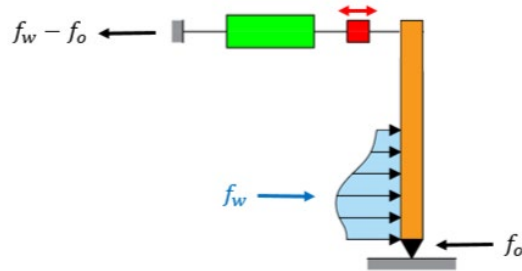
Figure 3-2. Static equilibrium for the force at the top of the cylinder for the hold case.
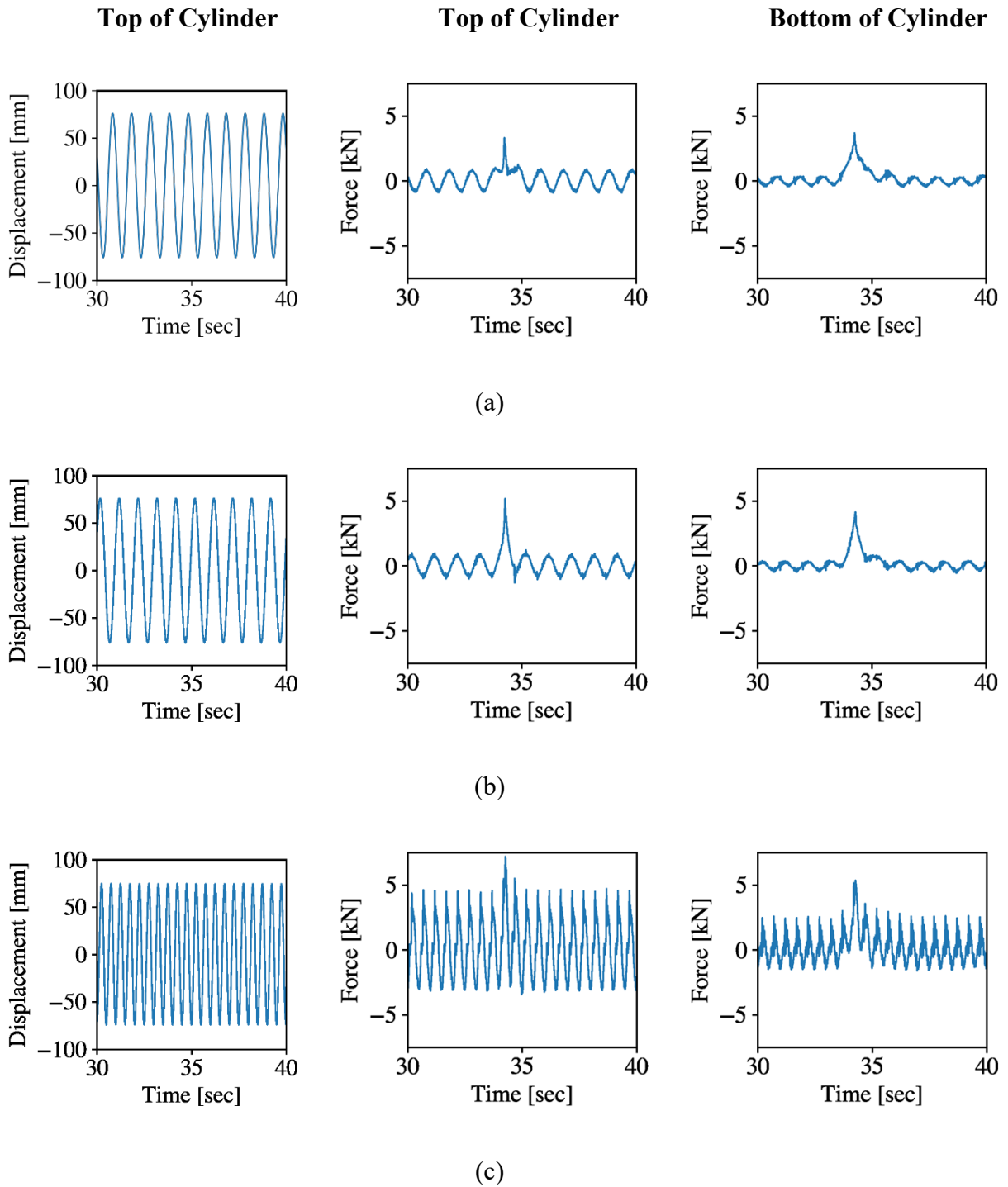
3.2. Sinusoidal Wave Loading

A second round of trials was performed to study the interaction of a moving structure with the hydrodynamic loading. Additionally, this testing phase ensured proper communication between the sensors and data-acquisition system. Two continuous sinusoidal waves with frequencies of 1 Hz and 2 Hz and an amplitude of 76.2 mm (3 inches) were applied to the specimen using the actuator and controller during the wave loading. The initial forces to push the cylinder back and forth came from inertia, water sloshing at the base of the cylinder, potential actuator dynamics, flexibility of the transfer frame, and friction between the specimen and clevises.

Superposition can be observed in figure 3-3, resulting from the force from the wave loading and the force needed to move the cylinder to the specified displacement. This superposition is illustrated in terms of dynamic equilibrium in figure 3-5. If the wave reached the cylinder near the time of peak displacement when the cylinder was moving toward the wavemaker from its farthest displaced position from the wavemaker (positive displacement, negative velocity values), then the two forces combined and resulted in a larger force at the top of the cylinder. Conversely, if the wave reached the cylinder near the time of peak displacement when the cylinder was moving toward the wavemaker to its closest displaced position to the wavemaker (negative displacement, negative velocity values), then the two forces combined to result in a smaller force at the top of the cylinder. A peak force value of 3.32 kN was measured for Trial 18, highlighting the superposition principle. The peak values of force at the top of the cylinder for trials 21 and 22 were 5.17 kN and 7.18 kN, respectively, which were noticeably larger than those of trials 16 and 17 for the hold case. At the bottom of the cylinder, the peak values for trials 18, 21, and 22 were 3.53 kN, 3.99 kN, and 5.21 kN, respectively. In all three of these cases, velocities were negative and corresponded to when the cylinder was moving toward the wavemaker.

The force applied to the specimen from the tsunami wave during these trials was jointly dependent on the displacement and velocity of the cylinder at the time of impact; see figure 3-4. Velocities were calculated from the displacements by using the approximate derivative from the central difference method. The time of peak force (at either the top or bottom of the cylinder) was used to define the displacement and velocity values for these plots. While there were not enough data points to draw conclusions, trends were observed:

(1) Forces at the top of the cylinder were smaller when the cylinder was displaced closest to the wavemaker and larger when the cylinder was displaced farthest from the wavemaker, as illustrated by superposition between the applied force needed to reach the desired displacement, $f_a(u)$, and the wave loading, f_w, in figure 3-5 (a,b) (trials 18-20 versus trials 21-22).

(2) Forces generally increased with increasing velocity when the cylinder was moving toward the wavemaker when the actuator had to resist the applied wave loading to meet the target displacement, as illustrated by $f(v)$ in figure 3-5 (a or b). The largest forces at the top of the cylinder still occurred near the farthest displaced position because of the aforementioned superposition effects shown in figure 3-5 (a) (trials 18, 20-22).

(3) The smallest force at the top of the cylinder occurred when the cylinder was moving away from the wavemaker toward zero displacement and was not near a peak displacement value when the wave "helped" the actuator move toward the target displacement. This was not true of the force at the bottom of the cylinder (Trial 19 was the only trial exhibiting this behavior).

(4) Forces were fairly consistent at the bottom of the cylinder for the 1 Hz case.

(5) Forces and velocities were significantly different for the 2-Hz case in comparison to the 1-Hz cases at approximately the same displacement, indicating larger peak measured forces with higher frequency/velocity.

Top of Cylinder **Top of Cylinder** **Bottom of Cylinder**

(a)

(b)

(c)

Figure 3-3. Displacement at the top of the cylinder, force at the top of the cylinder, and force at the bottom of the cylinder for sinusoidal wave loading: (a) Trial 18 (1 Hz), (b) Trial 21 (1 Hz), (c) Trial 22 (2 Hz).
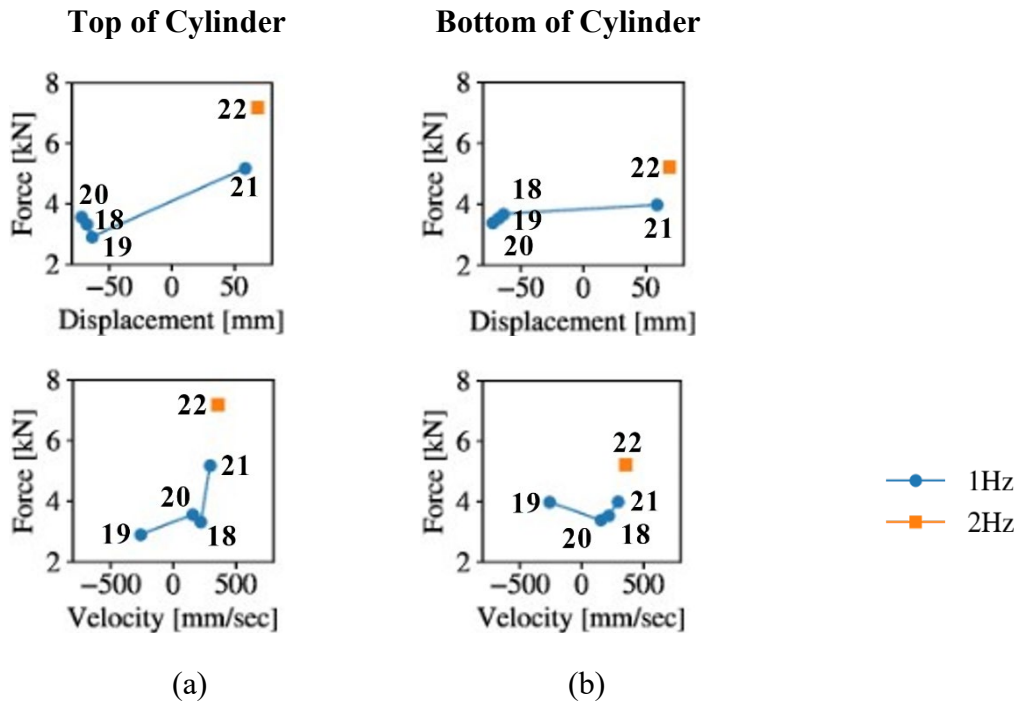
Figure 3-4. Sine wave loading for trials 18, 19, 20, 21 (1Hz) and Trial 22 (2Hz): (a) Peak force vs. displacement/velocity at the top of the cylinder, (b) Peak force vs. displacement/velocity at the bottom of the cylinder.

$$ma = f_w - f_o + f_a(u) - f(v)$$

moving away from wavemaker

$$ma = f_w - f_o - f_a(u) - f(v)$$

moving away from wavemaker

$$ma = f_w - f_o + f_a(u) + f(v)$$

moving towards wavemaker

$$ma = f_w - f_o - f_a(u) + f(v)$$

moving towards wavemaker

(a)   (b)
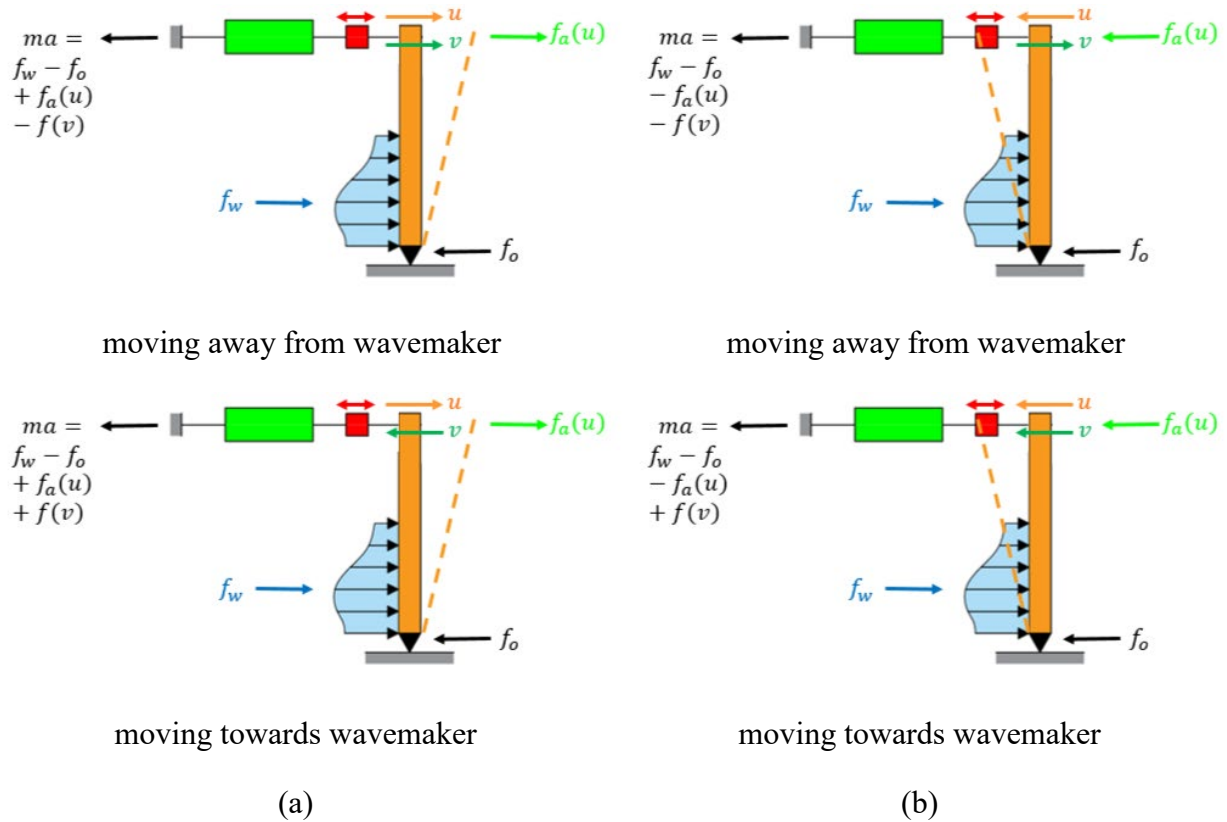
Figure 3-5. Dynamic equilibrium for force at the top of the cylinder for the sine case: (a) near the farthest displacement from the wavemaker, (b) near the closest displacement to the wavemaker.

3.3. Real-Time Hybrid Simulation

Selected trials are presented to highlight differences in loading scenarios with different seismic loading; see figure 3-6.

Trial 03 represented the hydro-RTHS only dataset without previous damage from seismic loading. Displacements of 5.55 mm were observed for this trial; this loading did not include additional scaling to approximate larger wave forces due to a higher density of debris; comparisons with Trial 09 indicated that the difference in displacement response was larger when the higher density of the tsunami wave was accounted for; see figure 3-6 (a) v. (c). Trial 09 showed that the 1.5 factor resulteds in a near-proportional increase in the displacements relative to Trial 03 (by 1.37 times), which used a 1.0 scale factor for the waves. The first-mode structural period was 1.16 seconds in the transverse direction, approximately corresponding to the duration of the wave loading.
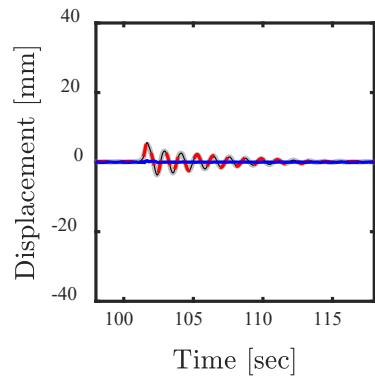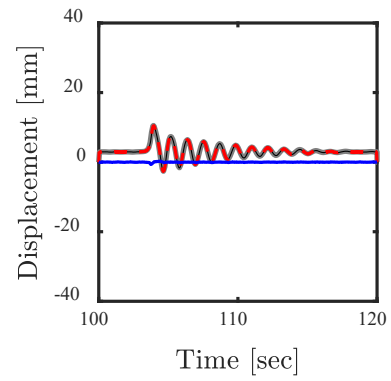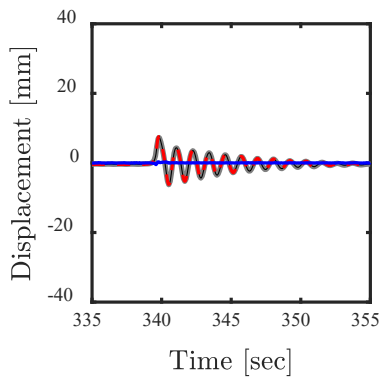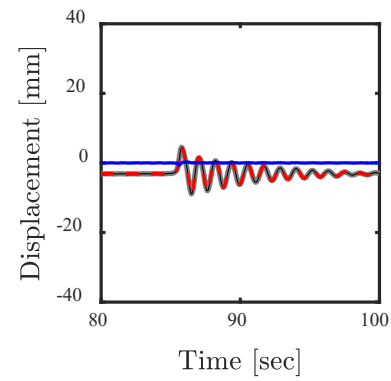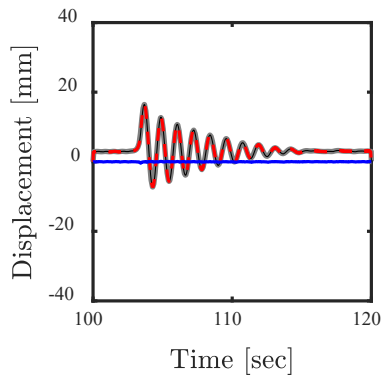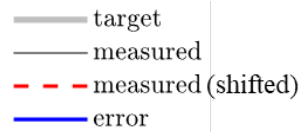
Figure 3-6. RTHS command and measured displacements at the top of the cylinder: (a) Trial 03, (b) Trial 06, (c) Trial 09, (d) Trial 10, (e) Trial 19.

Trials 06 and 19 both used the El Centro ground motion record, scaled up in magnitude by a factor of 2.0. These trials both used a scale factor of 1.5 for the forces to account for the higher density of tsunami waves. The notable difference between the two runs was that Trial 06 was performed with the tsunami loading applied to only one of the two bridge piers after the seismic event, while Trial 19 applied the tsunami loading to both bridge piers. The maximum amplitude for Trial 06 was 7.62 mm, relative to the residual seismic displacement, while the loading applied to both bridge piers for Trial 19 was 13.72 mm, relative to the residual seismic displacement, approximately double that of the loading of a single bridge pier (a factor of 1.8); see figure 3-6 (b) vs. (e). The forces for these two trials also increased relative to the scale factor; see figure 3-7 (b, e).

Trials 06, 09, and 10 compared changes in the dynamic response from the wave loading due to previous damage from the seismic loading for different ground motions. An additional trial using the JMA Kobe ground motion record is not shown (Trial 08), as the observed displacements under the seismic loading exceeded the valid range of the numerical model. The amplitude of the displacement relative to the residual displacement after the seismic loading remained approximately 7.62 mm for the wave loading, regardless of previous seismic damage. However, the post-wave oscillations had slight period elongation from the damaged bridge specimen.

After exhibiting inelastic response for the seismic loading, all trials remained in the linear-elastic range for the subsequent wave loading. Figure 3-8 plots the moment-rotation of the SSI spring at the bottom of the piers, which remained in the linear-elastic range for all the trials because of its low stiffness. Figure 3-9 plots the force-deformation response of the abutments, which exhibited substantial nonlinear response for the seismic loading but remained elastic for the tsunami loading. In particular, the coupled plasticity properties of the elastomeric bearing element was exhibited in Trial 10 for the large displacements induced by the Takatori ground motion record; see figure 3-9 (d). Since the left and right abutments had a nearly identical force-deformation history, only the left is shown. Future work will investigate structural properties that exhibit nonlinear behavior for the wave loading.
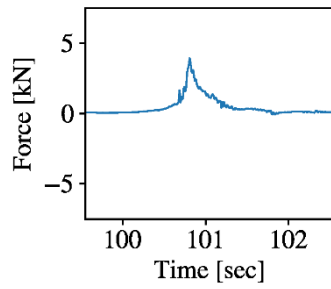
Force at top of cylinder　　　　　**Force at bottom of cylinder**
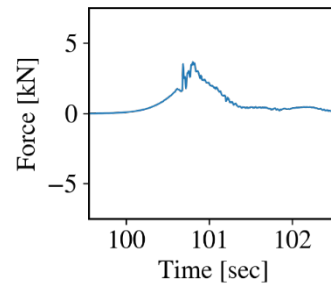
(a)
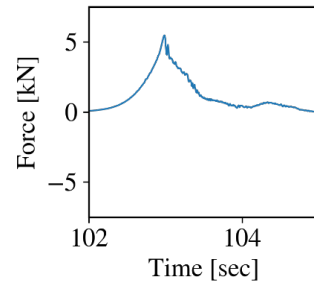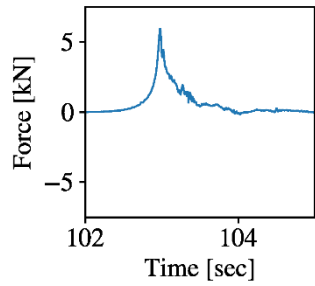
(b)
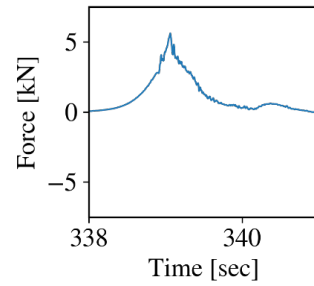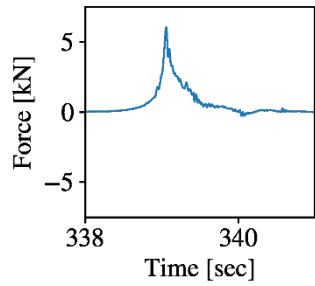
(c)
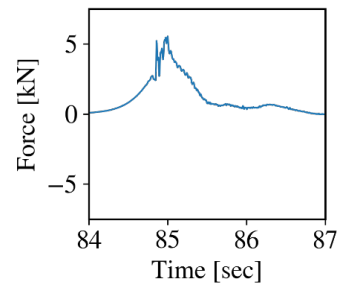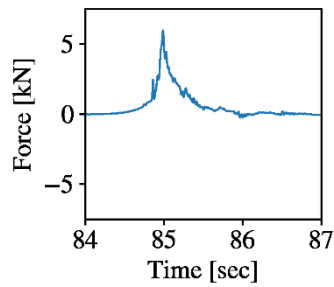
(d)

Figure 3-7. RTHS force at the top of the cylinder and force at the bottom of the cylinder: (a) Trial 03, (b) Trial 06, (c) Trial 09, (d) Trial 10, (e) Trial 19.
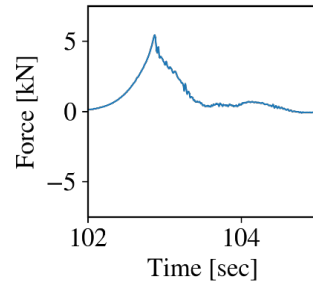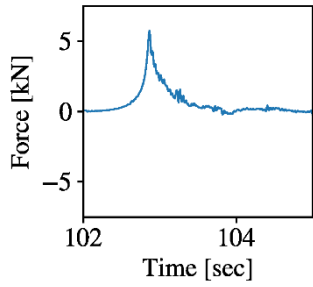
(e)

3-7 continued. RTHS force at the top and bottom of the cylinder: (a) Trial 03, (b) Trial 06, (c) Trial 09, (d) Trial 10, (e) Trial 19.
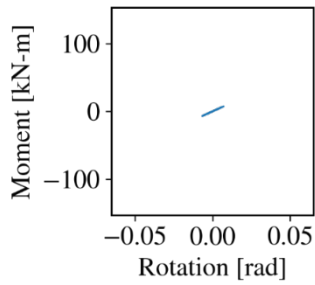
(a)
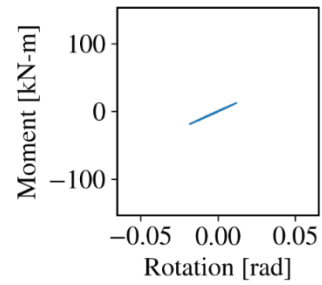
(b)
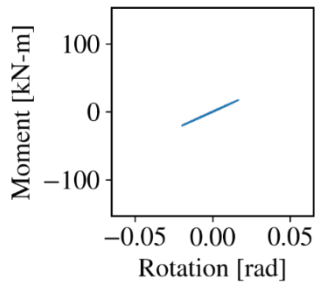
(c)
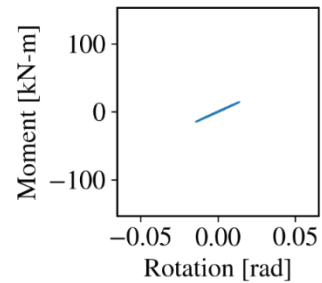
(d)
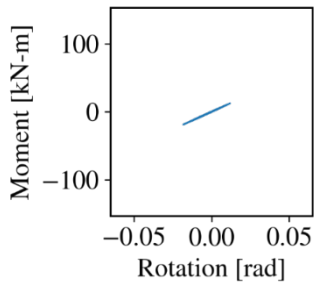
(e)

Figure 3-8. Hysteretic loop of numerical SSI spring at base of the pier for seismic and wave loading: (a) Trial 03, (b) Trial 06, (c) Trial 09, (d) Trial 10, (e) Trial 19.

Seismic and wave loading   **Wave loading only**
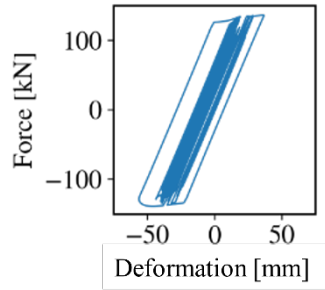
(a)
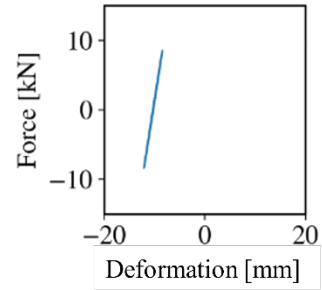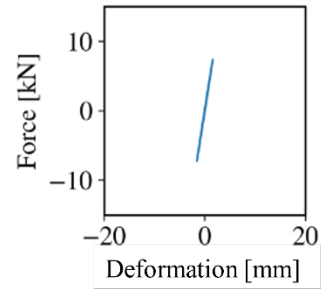
(b)
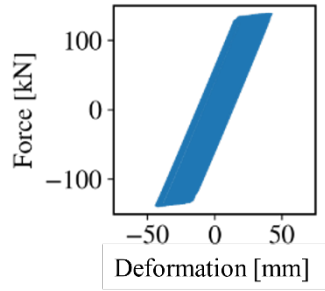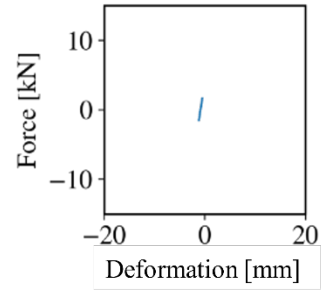
(c)
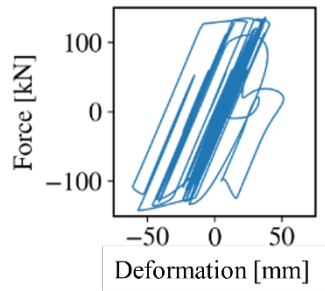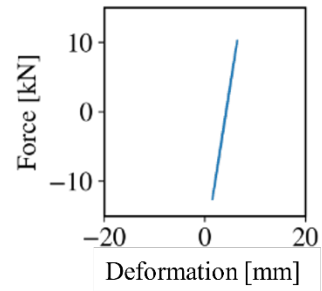
(d)
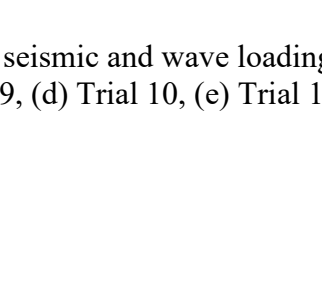
Figure 3-9. Hysteretic loop of numerical abutment for the seismic and wave loading and wave loading only: (a) Trial 03, (b) Trial 06, (c) Trial 09, (d) Trial 10, (e) Trial 19.

<center>(e)</center>

3-9 continued. Hysteretic loop of numerical abutment for seismic and wave loading and wave loading only: (a) Trial 03, (b) Trial 06, (c) Trial 09, (d) Trial 10, (e) Trial 19.

The forces recorded in OpenSees at the top and bottom of the cylinder were ~50 percent larger than those recorded for the hold loading case, corresponding to the 1.5 scale factor (see figure 3-7). Without said scaling, the maximum force at the top of the cylinder for Trial 03 for the pure hydro-RTHS case matched that of Trial 17 for the hold case near the same value of 3.92 kN; see (a) vs. figure 3-1 (b). At the top of the cylinder, all hydro-RTHS trials had maximum values similar to that of the hold case when the 1.5 scaling was accounted for between 3.82 kN for Trial 19 to 4.03 kN for Trial 09. However, the forces at the bottom of the cylinder were slightly larger than those recorded for the hold case when for scaling was accounted for, with a minimum of 3.63 kN for Trial 19 and a maximum of 3.75 kN for Trial 09. Results indicated that the peak forces measured in the experiment for this particular bridge were relatively independent of the motion and oscillations induced by the wave loading, implying that the hybrid simulation could have been conducted in an offline manner and resulted in similar results. Further work is needed to determine cases when this motion affects the wave loading magnitude.

3.4. Assessment of Hydro-RTHS

The blue line in figure 3-6 shows the error between the measured and target displacements at the top of the specimen. Only small errors were exhibited at the instant of wave impact; e.g., figure 3-6 (b) shows the largest error of ~0.64 mm. The free vibration response exhibited even smaller errors between the command and target displacements. In all of the trials, real-time computations in the numerical sub-assembly were executed within the allotted time step constraints; i.e., the predictor-corrector algorithm did not compensate for delays in receiving commands from the finite-element model; e.g., see figure 3-10 (f), which indicates states only

<center>41</center>

between values of 0 and 1. The ATS compensator performed very well; peak time delays in the time series were minimal and observed in msec only for Trial 03 and Trial 09 (see table 2-4). The peak value of the normalized root-mean-square (RMS) error is also shown in table 2-4, indicating small errors, all below 1 percent. This RMS error was normalized by dividing it over the range between the maximum and minimum values of displacement.

A variety of error plots from the target machine are presented for final Trial 19 in figure 3-10, showing good performance of the hydro-RTHS testing method. The error with respect to time is shown in figure 3-10 (a), indicating that the largest spike in error occurred near the time of initial wave impact. Fast Fourier Transform (FFT) of the error indicated a peak around the frequency associated with the test setup of around 54.3 Hz [figure 3-10 (b)]; this frequency was significantly higher than the longitudinal and transverse frequencies of interest in the bridge model. The subplot shown in figure 3-10 (c) exhibits a near 45 degree slope, indicating good tracking between the command and target displacements. The tracking indicator (Mercan and Ricles 2007) in figure 3-10 (d) is negative for the majority of the loading, indicating very small values of lag measured behind the command signal; similarly the RMS error is positive and well-below 1 percent in figure 3-10 (e). The state of the predictor-corrector subplot in figure 3-10 (e) shows that all calculations for the command displacement were evaluated within the assigned time step (State 1) and did not have to compensate for delays (State 2; not shown).

3.5.   Preliminary Validation of Hydro-RTHS Results

Initial validation of the hydro-RTHS testing was conducted by comparing additional sensor data with data from the numerical model; see figure 3-11. Comparisons with the load cell measurements at the base of the pier and the reactions extracted from the numerical sub-assembly indicated that equilibrium was approximately satisfied between the numerical and physical sub-assemblies using the partitioning scheme in figure 2-7.
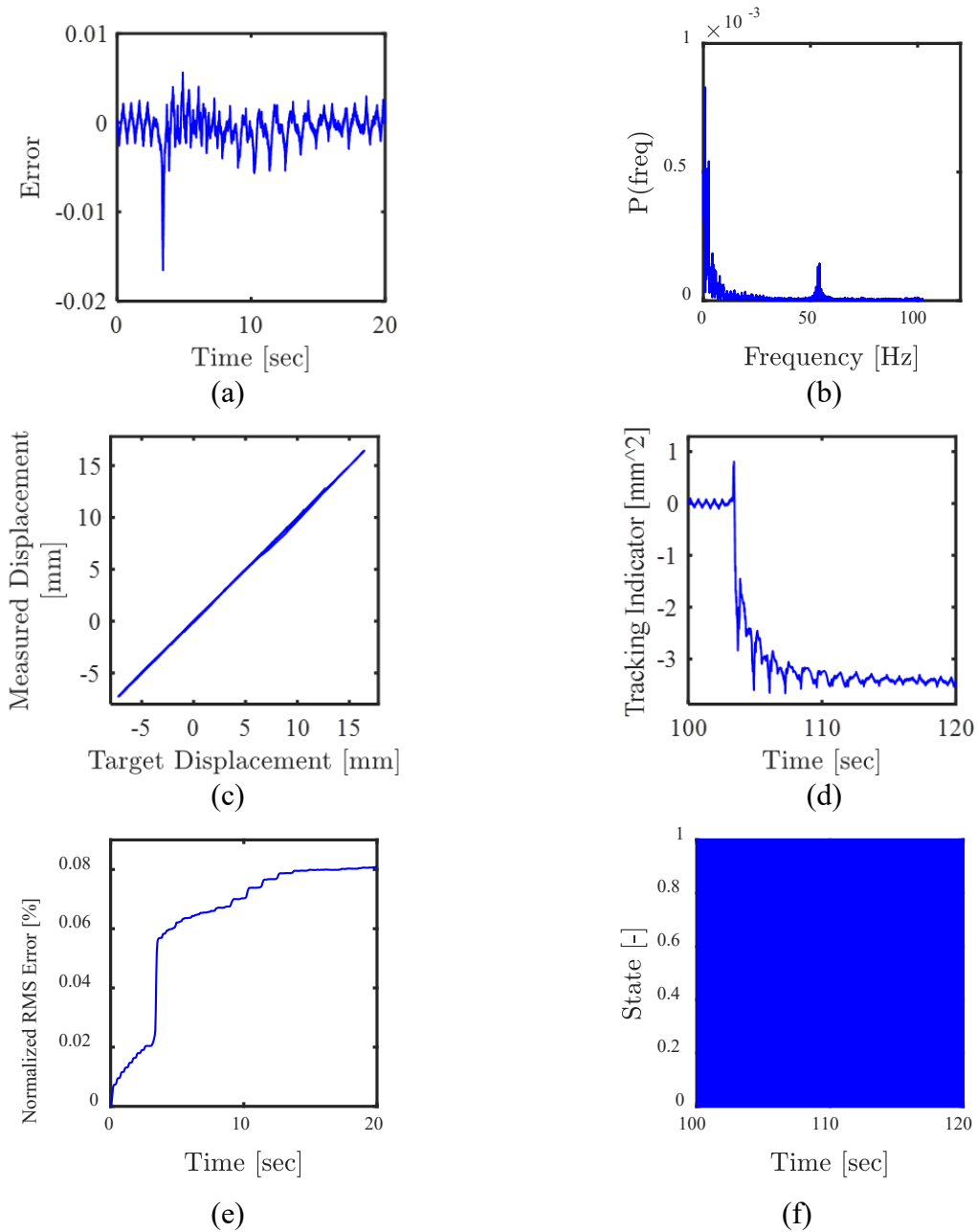
Figure 3-10. Target machine error plots for Trial 19: (a) Error between measured and target displacement, (b) FFT of error between the measured and target displacement – Frequency domain, (c) Subspace plot of the measured vs. target displacement, (d) Tracking indicator of the measured vs. target displacement, (e) Normalized RMS error between the measured and target displacement, (f) State of the predictor-corrector.
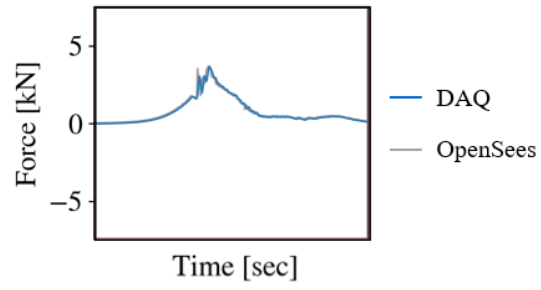
Figure 3-11. Comparison of reaction at the cylinder base for Trial 03.

CHAPTER 4. CONCLUSIONS

These experiments aimed to illustrate the feasibility of using hydro-RTHS as a means for improving understanding of wave-structure interaction, as well as to make hydro-RTHS a valuable testing method for the future development of datasets to validate computational models of nonlinear hydrodynamics and fluid-structure interaction. A cylindrical test specimen representing a typical bridge pier was coupled to a three-span numerical model of a bridge, including SSI effects. The coupled physical-numerical model was numerically subjected to seismic loading followed by physical wave loading at Oregon State University's Large Wave Flume using a three-tier RTHS testing architecture. Low error and small time delays were calculated between the measured and target displacement of the specimen. Additional load cell information from the experiment and numerical model was used as preliminary validation of the hydro-RTHS results.

After initial wave impact, the hydro-RTHS tests exhibited free vibration response. Regardless of the damage imparted by the initial seismic loading, which exhibited nonlinear response at the abutments, the numerical sub-assembly remained elastic for the wave loading conditions. Future work will investigate this response with refined and more realistic numerical sub-assemblies that also include inelastic response. Impact to a bridge deck instead of a cylindrical bridge pier, which has a larger impact area, would also result in a more marked response during the wave loading than that presented in this pilot study (Bradner et al. 2011, Xiang et al. 2020).

Although peak responses remained similar for the wave loading, previous damage from the earthquake resulted in slightly elongated periods in the free vibration phase of the structural model. Force response for hydro-RTHS was similar to the hold case without hydro-RTHS when scaling of the wave loading (to account for the higher density of salt water and debris associated with tsunami waves) was not applied, and it increased by the equivalent multiplier when scaling of the wave force was included. This indicated that the motion of the pier little affected the applied wave loading for the structural model considered herein. This result implies that this specific study could have been conducted offline, with the wave loading extracted from the experiment and applied in a numerical model, but this may not be the case for every structural and wave type. For example, the forces measured for the case when the actuator imposed a larger, sinusoidal displacement at the top of the pier were dependent on the displacement and

velocity of the specimen at the time of wave impact, indicating two-way effects between the fluid and structure.

Although the numerical model of the bridge was highly idealized, this research demonstrates the feasibility of using RTHS for wave-structure interaction problems. The three-span bridge, including flexibility at the base of the pier due to SSI and previous earthquake damage, would be impossible to model in existing hydrodynamic facilities without the hydro-RTHS testing method. Future work will investigate the use of more complex bridge models with nonlinear response during the wave loading. Differences in scaling laws between the numerical and physical sub-assemblies, e.g., via Froude scaling, will also be investigated. Note, if similitude is investigated, the numerical sub-assembly will need to conduct calculations faster than real time to match the timescale of the scaled down physical model. These future studies will yield data for cascading seismic and tsunami loadings for bridges in greater detail than what is currently feasible without hydro-RTHS.

REFERENCES

AASHTO. (1996). Standard Specifications for Highway Bridges. *Sixteenth*. Washington D.C.: American Association of State Highway and Transportation Officials, Inc.

Akiyama, M. Frangopol, D. M. Arai, M. and Koshimura, S. (2012). Probabilistic assessment of structural performance of bridges under tsunami hazard. *Structures Congress 2012* (pp. 1919-1928). Reston, VA: ASCE.

Aviram, A. Schellenberg, A. and Stojadinovic, B. (2012). Seismic Design and Performance of Two Isolation Systems Used for Reinforced Concrete Bridge Construction. *15th World Conference on Earthquake Engineering.* Lisbon, Portugal: Sociedade Portuguesa de Engenharia Sismica (SPES).

Azadbakht, M. and Yim, S. C. (2015). Simulation and estimation of tsunami loads on bridge superstructures. *Journal of Waterway, Port, Coastal, and Ocean Engineering 141*(2) 04014031. Retrieved from https://doi.org/10.1061/(ASCE)WW.1943-5460.0000262

Azadbakht, M. and Yim, S. C. (2016). Estimation of Cascadia Local Tsunami Loads on Pacific Northwest Bridge Superstructures. *Journal of Bridge Engineering 21*(1) 04015048. Retrieved from http://dx.doi.org/10.1061/(ASCE)BE.1943-5592.0000755

Baker, J. W. Lin, T. and Shahi, S. K. (2011). *New Ground Motion Selection Procedures and Selected Motions for the PEER Transportation Research Program.* Berkeley: Pacific Earthquake Engineering Research Center.

Bayati, I. Facchinetti, A. Fontanella, A. Giberti, H. and Belloli, M. (2018). A wind tunnel/HIL setup for integrated tests of Floating Offshore Wind Turbines. *Journal of Physics: Conference Series 1037* 052025.

Bayer, V. Dorka, U. Fuellekrug, U. and Gschwilm, J. (2005). On real-time pseudo-dynamic sub-structuring testing: algorithm, numerical and experimental results. *Aerospace Science and Technology 9*(3) 223-232.

Bozorgnia, Y. (2020). *Data Resources for NGA-Subduction Project.* Berkeley: Pacific Earthquake Engineering Research Center. Retrieved from https://peer.berkeley.edu/sites/default/files/2020_02_final_3.17.2020.pdf

Bradner, C. Schumacher, T. Cox, D. and Higgins, C. (2011). Experimental Setup for a Large-Scale Bridge Superstructure Model Subjected to Waves. *Journal of Waterway, Port,*

Coastal, and Ocean Engineering 137(1) 3-11. doi:10.1061/(ASCE)WW.1943-5460.0000059

Caltrans. (2004). Caltrans Seismic Design Criteria. *Version 1.3*. Sacramento CA: California Department of Transportation.

Carey, T. J. Mason, H. B. Barbosa, A. R. and Scott, M. H. (2019). Multihazard Earthquake and Tsunami Effects on Soil-Foundation-Bridge Systems. *Journal of Bridge Engineering 24*(4) 04019004. Retrieved from https://doi.org/10.1061/(ASCE)BE.1943-5592.0001353

Carrion, J. E. and Spencer, B. F. (2007). *Series Model-Based Strategies for Real-Time Hybrid Testing.* University of Illinois. Urbana-Champaign, IL: NSEL Report.

Chabaud, V. Steen, S. and Skjetne, R. (2013). Real-time hybrid testing for marine structures: challenges and strategies. *ASME 2013 32nd International Conference on Ocean, Offshore and Arctic Engineering 5.* Nantes, France. doi:10.1115/OMAE2013-10277

Chae, Y. Kazemibidokhti, K. and Ricles, J. M. (2013). Adaptive time series compensator for delay compensation of servo-hydraulic actuator systems for real-time hybrid simulation. *Earthquake Engineering & Structural Dynamics 42* 1697-1715. doi:10.1002/eqe.2294

Dorka, U. E. (2002). Hybrid experimental - numerical simulation of vibrating structures. *International Conference WAVE2002.* Okayama, Japan.

Dorka, U. E. and Heiland, D. (1991). Fast Online Earthquake Utilitzing a Novel PC Supported Measurement and Control Concept. *4th Conference on Structural Dynamics.* Southampton, UK.

Hall, M. (2016). *Hybrid Modeling of Floaring Wind Turbines.* University of Maine, Orono ME: Ph.D. dissertation.

Hall, M. and Goupee, A. J. (2018). Validation of a hybrid modeling approach to floating wind turbine basin testing. *Wind Energy 21*(6) 391-408.

Hughes, T. J. Pister, K. S. and Taylor, R. L. (1979). Implicit-explicit finite elements in nonlinear transient analysis. *Computer Methods in Applied Mechanics and Engineering 17-18* 159-182. Retrieved from https://doi.org/10.1016/0045-7825(79)90086-0

Hulbert, G. M. and Chung, J. (1996). Explicit Time Integration Algorithms for Structural Dynamics with Optimal Numerical Dissipation. *Computer Methods in Applied Mechanics and Engineering 137*(2) 175-188. Retrieved from https://doi.org/10.1016/S0045-7825(96)01036-5

Iemura, H. Pradono, M. H. and Takahashi, Y. (2005). Report on the tsunami damage on the bridges in Banda Aceh and some possible countermeasures. *28th JSCE Earthquake Engineering Symposium. 28.* Tokyo: Japan Society of Civil Engineers.

Kawashima, K. (2012). Damage of bridges due to the 2011 Great East Japan earthquake. *International Symposium Engineering Lessons Learned from the 2011 Great East Japan Earthquake* (pp. 82-101). Tokyo: Japan Association of Earthquake Engineering.

Ketchum, M. Chang, V. and Shantz, T. (2004). *Influence of Design Ground Motion Level on Highway Bridge Costs.* Berkeley: Pacific Earthquake Engineering Research Center.

Kolay, C. and Ricles, J. M. (2014). Development of a Family of Unconditionally Stable Explicit Direct Integration Algorithms with Controllable Numerical Energy Dissipation. *Earthquake Engineering & Structural Dynamics 43* 1361-1380. Retrieved from https://doi.org/10.1002/eqe.2401

Kolay, C. Ricles, J. M. Marullo, T. M. Al-Subaihawi, S. and Quiel, S. E. (2018, February). Computational Challenges in Real-Time Hybrid Simulation of Tall Buildings under Multiple Natural Hazards. *Key Engineering Materials 763* pp. 566-575. Retrieved from https://doi.org/10.4028/www.scientific.net/KEM.763.566

Krawinkler, H. Medina, R. and Alavi, B. (2003). Seismic Drift and Ductility Demands and their Dependence on Ground Motions. *Engineering Structures 25*(5) 637-653. Retrieved from https://doi.org/10.1016/S0141-0296(02)00174-8

La Mura, F. Todeschini, G. and Giberti, H. (2018). High Performance Motion-Planner Architecture for Hardware-In-the-Loop System Based on Position-Based-Admittance-Control. *Robotics 7*(1) 8.

Lomonaco, P. Maddux, T. Bosma, B. Myers, A. T. Arwade, S. A. Hallowell, S. and Johlas, H. M. (2019). Physical Model Testing of Wave Impact Forces on Fixed Foundations of Offshore Wind Turbines. *Twenty-ninth International Ocean and Polar Engineering Conference.* Honolulu, HI: International Society of Offshore and Polar Engineers (ISOPE).

Mahin, S. A. and Williams, M. E. (1980). Computer controlled seismic performance testing. *Dynamic Response of Structures: Experimentation, Observation, Prediction and Control.* New York, NY: American Society of Civil Engineers.

Maruyama, K. Tanaka, Y. and Hosoda, A. (2012). Damage of bridges structures by huge tsunami and evaluation of tsunami force on bridges. *8th International Symposium on Social Management Systems, SSMS2012 - Disaster Prevention and Reconstruction Management* (pp. 1-8). New York: United Nated Office for Disaster Risk Reduction.

McKenna, F. Scott, M. H. and Fenves, G. L. (2010). Nonlinear finite-element analysis software architecture using object composition. *Journal of Computing in Civil Engineering 24*(1) 95-107.

Mercan, O. and Ricles, J. (2007). Stability and accuracy analysis of outer loop dynamics in real-time pseudodynamic testing of SDOF systems. *Earthquake Engineering & Structural Dynamics 36*(11) 1523-1543. doi:https://doi.org/10.1002/eqe.701

Mosqueda, G. (2003). *Continuous hybrid simulation with geographically distributed substructures.* University of California, Berkeley, Berkeley CA: Ph.D. dissertation.

Nakashima, M. and Masaoka, N. (1999). Real-time on-line test for MDOF systems. *Earthquake Engineering & Structural Dynamics 28*(4) 393-420.

Nakashima, M. Kaminosono, T. Ishida, M. and Ando, K. (1990). Integration Techniques for Substructure Pseudo Dynamic Test. *Journal of Structural and Construction Engineering 417* 515-524.

Nakashima, M. Kato, H. and Takaoka, E. (1992). Development of Real-time Pseudo Dynamic Testing. *Earthquake Engineering & Structural Dynamics 21*(1) 79-92. Retrieved from https://doi.org/10.1002/eqe.4290210106

Newmark, N. M. (1959). A Method of Computation for Structural Dynamics. *Journal of the Engineering Mechanics Division 85*(3) 67-94. Retrieved from https://doi.org/10.1061/JMCEA3.0000098

Pan, P. Nakashima, M. and Tomofuji, H. (2005). Online test using displacement-force mixed control. *Earthquake Engineering & Structural Dynamics 34*(8) 869-888.

Park, H. Tomiczek, T. Cox, D. van de Lindt, J. and Lomonaco, P. (2017). Experimental modeling of horizontal and vertical wave forces on an elevated coastal structure. *Coastal Engineering 128* 58-74. Retrieved from https://doi.org/10.1016/j.coastaleng.2017.08.001

Robertson, I. Riggs, H. and Mohamed, A. (2008). Experimental results of tsunami bore forces on structures. *ASME 2008 27th International Conference on Offshore Mechanics and Arctic Engineering.* Estoril, Portugal: American Society of Mechanical Engineers.

Sauder, T. Chabaud, V. Thys, M. Bachynski, E. E. and Sæther, L. O. (2016). Real-Time Hybrid Model Testing of a Braceless Semi-Submersible Wind Turbine: Part I - The Hybrid Approach. *ASME 2016 35th International Conference on Ocean, Offshore and Arctic Engineering. 6.* Busan, South Korea: American Society of Mechanical Engineers. doi:10.1115/OMAE2016-54435

Schellenberg, A. Mahin, S. and Fenves, G. (2009). *Advanced Implementation of Hybrid Simulation.* University of California, Berkeley. Berkeley: Pacific Earthquake Engineering Research Center.

Shing, P. B. and Mahin, S. A. (1983). *Experimental error propagation in pseudodynamic testing.* Berkeley, CA: Earthquake Engineering Research Center.

Takanashi, K. Udagawa, K. Seki, M. Okada, T. and Tanaka, H. (1975). Non-linear earthquake response analysis of structures by a computer-actuator online system--Part 1: detail of the system. *Transactions of the Architectural Institute of Japan*(229) 77-83.

Tomiczek, T. Prasetyo, A. Mori, N. Yasuda, T. and Kennedy, A. (2016). Physical modelling of tsunami onshore propagation, peak pressures, and shielding effects in an urban building array. *Coastal Engineering 117* 97-112. Retrieved from https://doi.org/10.1016/j.coastaleng.2016.07.003

Traubita, A. A. (2009). *Structural Response and Cost Characterization of Bridge Construction using Seismic Performance Enhancement Strategies.* University of California, Berkeley, Berkeley CA: Ph.D. dissertation.

Vilsen, S. Sauder, T. Sørensen, A. and Føre, M. (2019). Method for Real-Time Hybrid Model Testing of ocean structures: Case study on horizontal mooring systems. *Ocean Engineering 172* 46-58.

Wu, B. Xu, G. Wang, Q. and Williams, M. S. (2006). Operator-Splitting Method for Real-Time Substructure Testing. *Earthquake Engineering & Structural Dynamics 35*(3) 293-314.

Wüthrich, D. Pfister, M. and Schleiss, A. (2016). Example of wave impact on a residential house. *Sustainable Hydraulics in the Era of Global Change: 4th IAHR Europe Congress.* Liege, Belgium: CRC Press.

Xiang, T. Istrati, D. Yim, S. C. Buckle, I. G. and Lomonaco, P. (2020). Tsunami Loads on a Representative Coastal Bridge Deck: Experimental Study and Validation of Design

Equations. *Journal of Waterway, Port, Coastal, and Ocean Engineering 146*(5)
04020022. doi:10.1061/(ASCE)WW.1943-5460.0000560

Yashinsky, M. (2012). Lessons for Caltrans from the 2011 Great Japan earthquake and tsunami.
*International Symposium Engineering Lessons Learned from the 2011 Great Japan
Earthquake* (pp. 1417-1428). Tokyo: Japan Association of Earthquake Engineering.

Yim, S. C. Wei, Y. Azadbakht, M. Nimmala, S. and Potisuk, T. (2015). Case Study for Tsunami
Design of Coastal Infrastructure: Spencer Creek Bridge, Oregon. *Journal of Bridge
Engineering 20*(1) 05014008. Retrieved from https://doi.org/10.1061/(ASCE)BE.1943-
5592.0000631

Zhong, W. (2005). *Fast Hybrid Test System for Substructure Evaluation.* University of Colorado,
Boulder CO: Ph.D. dissertation.

APPENDIX A

This appendix shows the timings for the various integration schemes that could potentially be used for hydro-RTHS. The tests explored alpha-OS, generalized-alpha-OS, Newmark for hybrid simulation with fixed iterations, and the Hilber-Hughes-Taylor method for hybrid simulation with fixed iterations. Additional variables included the number of iterations, system type, numberer type, and algorithm type. All runs were performed with plain constraints and transient analysis. A linear algorithm was used for all tests. The number of iterations was set to five for Newmark for hybrid simulation and Hilber-Hughes-Taylor for hybrid simulation. With the fixed iterations, the current version of OpenFresco indicated argument warnings, and results are not shown.

Case	System	Numberer	Integrator	Time (s)	Comments
AOS067 BGP	BandGeneral	Plain	AlphaOS (alpha = 0.67)	25.65782928	alpha = 2/3: Maximum damping. BandGen: Systems with banded profile.
AOS07 BGP	BandGeneral	Plain	AlphaOS (alpha = 0.7)	25.79377818	
AOS08 BGP	BandGeneral	Plain	AlphaOS (alpha = 0.8)	14.69704938	Convergence failure
AOS09 BGP	BandGeneral	Plain	AlphaOS (alpha = 0.9)	24.11335349	
AOS10 BGP	BandGeneral	Plain	AlphaOS (alpha = 1.0)	3.045375824	alpha = 1: No damping. Convergence failure
AOS067 BGRCM	BandGeneral	RCM	AlphaOS (alpha = 0.67)	25.49432254	
AOS07 BGRCM	BandGeneral	RCM	AlphaOS (alpha = 0.7)	25.36933303	
AOS08 BGRCM	BandGeneral	RCM	AlphaOS (alpha = 0.8)	14.54682875	Convergence failure
AOS09 BGRCM	BandGeneral	RCM	AlphaOS (alpha = 0.9)	24.42365265	
AOS10 BGRCM	BandGeneral	RCM	AlphaOS (alpha = 1.0)	3.214431524	Convergence failure
AOS067 PSPDP	ProfileSPD	Plain	AlphaOS (alpha = 0.67)	25.28876185	ProfSPD: Positive definite systems
AOS07 PSPDP	ProfileSPD	Plain	AlphaOS (alpha = 0.7)	25.02313209	
AOS08 PSPDP	ProfileSPD	Plain	AlphaOS (alpha = 0.8)	14.38189149	Convergence failure
AOS09 PSPDP	ProfileSPD	Plain	AlphaOS (alpha = 0.9)	24.17386341	
AOS10 PSPDP	ProfileSPD	Plain	AlphaOS (alpha = 1.0)	2.953168154	Convergence failure
AOS067 PSPDRCM	ProfileSPD	RCM	AlphaOS (alpha = 0.67)	25.3077569	
AOS07 PSPDRCM	ProfileSPD	RCM	AlphaOS (alpha = 0.7)	25.00196743	
AOS08 PSPDRCM	ProfileSPD	RCM	AlphaOS (alpha = 0.8)	14.4864943	Convergence failure
AOS09 PSPDRCM	ProfileSPD	RCM	AlphaOS (alpha = 0.9)	24.42809629	
AOS10 PSPDRCM	ProfileSPD	RCM	AlphaOS (alpha = 1.0)	2.939790487	Convergence failure

Figure A-1. Clocking of the five-span bridge model.

					UmfPack: Column pre-ordering strategy for unsymmetric-pattern multifrontal method.
AOS067 UPP	UmfPack	Plain	AlphaOS (alpha = 0.67)	26.09744143	Requires plain numberer.
AOS07 UPP	UmfPack	Plain	AlphaOS (alpha = 0.7)	26.12468338	
AOS08 UPP	UmfPack	Plain	AlphaOS (alpha = 0.8)	14.85998416	Convergence failure
AOS09 UPP	UmfPack	Plain	AlphaOS (alpha = 0.9)	24.82403827	
AOS10 UPP	UmfPack	Plain	AlphaOS (alpha = 1.0)	3.181134224	Convergence failure
AOSG00 BGP	BandGeneral	Plain	AlphaOSGeneralized (rhoInf = 0.0)	25.07177472	rhoInf = 0: Maximum numerical damping
AOSG01 BGP	BandGeneral	Plain	AlphaOSGeneralized (rhoInf = 0.1)	25.13032198	
AOSG02 BGP	BandGeneral	Plain	AlphaOSGeneralized (rhoInf = 0.2)	25.33750129	
AOSG03 BGP	BandGeneral	Plain	AlphaOSGeneralized (rhoInf = 0.3)	25.30836201	
AOSG04 BGP	BandGeneral	Plain	AlphaOSGeneralized (rhoInf = 0.4)	25.03456545	
AOSG05 BGP	BandGeneral	Plain	AlphaOSGeneralized (rhoInf = 0.5)	25.39124465	rhoInf = 0.5: AlphaOS (alpha = 2/3)
AOSG06 BGP	BandGeneral	Plain	AlphaOSGeneralized (rhoInf = 0.6)	26.38016772	
AOSG07 BGP	BandGeneral	Plain	AlphaOSGeneralized (rhoInf = 0.7)	9.101733208	Convergence failure
AOSG08 BGP	BandGeneral	Plain	AlphaOSGeneralized (rhoInf = 0.8)	4.533820152	Convergence failure
AOSG09 BGP	BandGeneral	Plain	AlphaOSGeneralized (rhoInf = 0.9)	4.736111641	Convergence failure
AOSG10 BGP	BandGeneral	Plain	AlphaOSGeneralized (rhoInf = 1.0)	3.260360956	rhoInf = 1.0: No numerical damping. Convergence failure
AOSG00 BGRCM	BandGeneral	RCM	AlphaOSGeneralized (rhoInf = 0.0)	24.21619606	
AOSG01 BGRCM	BandGeneral	RCM	AlphaOSGeneralized (rhoInf = 0.1)	24.31591916	
AOSG02 BGRCM	BandGeneral	RCM	AlphaOSGeneralized (rhoInf = 0.2)	24.2359488	
AOSG03 BGRCM	BandGeneral	RCM	AlphaOSGeneralized (rhoInf = 0.3)	24.78765965	
AOSG04 BGRCM	BandGeneral	RCM	AlphaOSGeneralized (rhoInf = 0.4)	24.57223845	
AOSG05 BGRCM	BandGeneral	RCM	AlphaOSGeneralized (rhoInf = 0.5)	25.66057444	
AOSG06 BGRCM	BandGeneral	RCM	AlphaOSGeneralized (rhoInf = 0.6)	24.84533548	
AOSG07 BGRCM	BandGeneral	RCM	AlphaOSGeneralized (rhoInf = 0.7)	9.214637995	Convergence failure
AOSG08 BGRCM	BandGeneral	RCM	AlphaOSGeneralized (rhoInf = 0.8)	4.165044785	Convergence failure
AOSG09 BGRCM	BandGeneral	RCM	AlphaOSGeneralized (rhoInf = 0.9)	4.104755402	Convergence failure
AOSG10 BGRCM	BandGeneral	RCM	AlphaOSGeneralized (rhoInf = 1.0)	2.920702219	Convergence failure

Figure A-1 continued. Clocking of the five-span bridge model.

			AlphaOSGeneralized		
AOSG00 PSPDP	ProfileSPD	Plain	(rhoInf = 0.0)	23.95939636	
AOSG01 PSPDP	ProfileSPD	Plain	AlphaOSGeneralized (rhoInf = 0.1)	25.19346356	
AOSG02 PSPDP	ProfileSPD	Plain	AlphaOSGeneralized (rhoInf = 0.2)	24.06353974	
AOSG03 PSPDP	ProfileSPD	Plain	AlphaOSGeneralized (rhoInf = 0.3)	25.367769	
AOSG04 PSPDP	ProfileSPD	Plain	AlphaOSGeneralized (rhoInf = 0.4)	24.34631777	
AOSG05 PSPDP	ProfileSPD	Plain	AlphaOSGeneralized (rhoInf = 0.5)	25.38076329	
AOSG06 PSPDP	ProfileSPD	Plain	AlphaOSGeneralized (rhoInf = 0.6)	25.17516589	
AOSG07 PSPDP	ProfileSPD	Plain	AlphaOSGeneralized (rhoInf = 0.7)	8.895128965	Convergence failure
AOSG08 PSPDP	ProfileSPD	Plain	AlphaOSGeneralized (rhoInf = 0.8)	4.047791004	Convergence failure
AOSG09 PSPDP	ProfileSPD	Plain	AlphaOSGeneralized (rhoInf = 0.9)	4.122744322	Convergence failure
AOSG10 PSPDP	ProfileSPD	Plain	AlphaOSGeneralized (rhoInf = 1.0)	2.943571329	Convergence failure
AOSG00 PSPDRCM	ProfileSPD	RCM	AlphaOSGeneralized (rhoInf = 0.0)	24.51734328	
AOSG01 PSPDRCM	ProfileSPD	RCM	AlphaOSGeneralized (rhoInf = 0.1)	23.86996317	
AOSG02 PSPDRCM	ProfileSPD	RCM	AlphaOSGeneralized (rhoInf = 0.2)	24.08126855	
AOSG03 PSPDRCM	ProfileSPD	RCM	AlphaOSGeneralized (rhoInf = 0.3)	24.73150659	
AOSG04 PSPDRCM	ProfileSPD	RCM	AlphaOSGeneralized (rhoInf = 0.4)	24.69049907	
AOSG05 PSPDRCM	ProfileSPD	RCM	AlphaOSGeneralized (rhoInf = 0.5)	24.90834475	
AOSG06 PSPDRCM	ProfileSPD	RCM	AlphaOSGeneralized (rhoInf = 0.6)	25.74824882	
AOSG07 PSPDRCM	ProfileSPD	RCM	AlphaOSGeneralized (rhoInf = 0.7)	8.885423422	Convergence failure
AOSG08 PSPDRCM	ProfileSPD	RCM	AlphaOSGeneralized (rhoInf = 0.8)	4.042680502	Convergence failure
AOSG09 PSPDRCM	ProfileSPD	RCM	AlphaOSGeneralized (rhoInf = 0.9)	4.088169336	Convergence failure
AOSG10 PSPDRCM	ProfileSPD	RCM	AlphaOSGeneralized (rhoInf = 1.0)	2.921326637	Convergence failure
AOSG00 UPP	UmfPack	Plain	AlphaOSGeneralized (rhoInf = 0.0)	26.016397	
AOSG01 UPP	UmfPack	Plain	AlphaOSGeneralized (rhoInf = 0.1)	25.5803864	
AOSG02 UPP	UmfPack	Plain	AlphaOSGeneralized (rhoInf = 0.2)	26.10298347	
AOSG03 UPP	UmfPack	Plain	AlphaOSGeneralized (rhoInf = 0.3)	25.56024623	
AOSG04 UPP	UmfPack	Plain	AlphaOSGeneralized (rhoInf = 0.4)	25.7189436	
AOSG05 UPP	UmfPack	Plain	AlphaOSGeneralized (rhoInf = 0.5)	26.12433147	
AOSG06 UPP	UmfPack	Plain	AlphaOSGeneralized (rhoInf = 0.6)	26.17897296	
AOSG07 UPP	UmfPack	Plain	AlphaOSGeneralized (rhoInf = 0.7)	9.374247789	Convergence failure
AOSG08 UPP	UmfPack	Plain	AlphaOSGeneralized (rhoInf = 0.8)	4.244928837	Convergence failure
AOSG09 UPP	UmfPack	Plain	AlphaOSGeneralized (rhoInf = 0.9)	4.29945159	Convergence failure
AOSG10 UPP	UmfPack	Plain	AlphaOSGeneralized (rhoInf = 1.0)	3.02200985	Convergence failure

Figure A-1 continued. Clocking of the five-span bridge model.

APPENDIX B

This appendix shows the recorded timings for the numerical evaluation of seismic loading on the reference five-span bridge using parallel processing. Nine cores gave the optimum speedups due to communication between cores.

Table B-1. Parallel processing clocks.

Number of Cores	Time [μs]
1	100396141
2	71780213
3	79878400
4	65698804
8	63983456
9	62822123
10	66298730

OpenSeesSP 2.5.0, OpenFresco 2.7.0, Tcl 8.5.18,
Message Passing Interface (MPI) mpich2-1.4.1p1,
System of equations Mumps,
Integrator AlphaOSGeneralized 0.9

To run OpenSeesSP, use (e.g., for nine processors):

```
mpiexec -n 9 OpenSeesSP.exe ThreeSpanBridge_master.tcl
```

To run with OpenFresco, run mpiexec command within OpeSeesSP.exe, tg.start in Simulink, and proceed with hybrid simulation. Below shows sample pseudo-code to set up an example bridge model. Code specific to parallel processing is highlighted in grey.

1. Initialize

```
# create log file
logFile $outDIR/ThreeSpanBridge.log

# define units
defaultUnits -force kip -length in -time sec -temp F
```

2. Build numerical sub-assembly.

```
# create ModelBuilder (with three-dimensions and 6 DOF/node)
model BasicBuilder -ndm 3 -ndf 6

# Define geometry for model
…

# Define bridge deck
…

# Define piers
```

```
…

# Define abutments
…

# Define foundation
…
```

3. Define experimental element with control type, SCRAMNetGT.

```
# define generic element tag
set genericTag 100

# create ModelBuilder (with three-dimensions and 6 DOF/node)
# model BasicBuilder -ndm 3 -ndf 6

## Load OpenFresco package
# (make sure all dlls are in the same folder as openSees.exe)
loadPackage OpenFresco

## Define experimental control
# expControl SCRAMNetGT $tag memOffset numDOF <-nodeID>
expControl SCRAMNetGT 1 4096 6 -nodeID 10;

## Define experimental setup
# expSetup NoTransformation $tag <-control $ctrlTag> -dof $DOFs -sizeTrialOut
$t $o <-trialDispFact $f> ...
# expSetup NoTransformation 1 -control 1 -dir 1 2 -sizeTrialOut 2 2; # 1 pier
expSetup NoTransformation 1 -control 1 -dof 1 2 3 4 -sizeTrialOut 4 4; # 2
piers

## Define experimental site
# expSite LocalSite $tag $setupTag
expSite LocalSite 1 1

## Define experimental elements
# expElement generic $eleTag -node $Ndi $Ndj ... -dof $dofNdi -dof $dofNdj ...
-site $siteTag -initStif $Kij <-iMod> <-noRayleigh> <-mass $Mij>

set kInit 0.0

# 1 pier
# expElement generic 100 -node 2 9 -dof 2 -dof 2 -site 1 -initStif $kInit -
$kInit -
$kInit $kInit -noRayleigh -checkTime

# 2 piers
expElement generic 100 -node 2 9 3 10 -dof 2 -dof 2 -dof 2 -dof 2 -site 1 -
initStif 0.0 0.0 0.0 0.0 0.0 0.0 0.0 0.0 0.0 0.0 0.0 0.0 0.0 0.0 0.0 0.0 -noRayleigh -
checkTime
```

4. Define static loads.

```
# Define gravity loads
timeSeries Linear 1 -factor 1.0

# Create a Plain load pattern with a Linear TimeSeries
pattern Plain 1 1 {
  # Create nodal loads
  load 5 0.0 0.0 -13.81 0.0 0.0 0.0
  …
}
```

5. Perform eigenvalue analysis

```
set lambda [eigen -fullGenLapack 6]
…
```

```
wipeAnalysis
```

6. Define damping

```
# define Rayleigh damping
rayleigh $a0 0.0 0.0 $a1

# Get initial stiffness
Initialize
wipeAnalysis
```

7. Define gravity analysis

```
# Define number of steps reach the load level
set Nsteps 10

# Start of analysis generation
# create the system of equations
system Mumps
# create the DOF numberer
numberer Plain
# create the constraint handler
constraints Plain
# create the convergence test
test NormDispIncr 1.0e-12 25
# create the integration scheme
integrator LoadControl [expr 1/$Nsteps]
# create the solution algorithm
algorithm Linear
# create the analysis object
analysis Static

# create recorder objects for gravity
…
```

8. Partitioning for parallel to keep experimental element from moving to different processors due to dynamic load balancing

```
# keep experimental element on partition p0
partition $genericTag
```

Note: This command is placed right before the analysis.

9. Apply static loads

```
# perform the gravity load analysis
record
analyze $Nsteps

# Set the gravity loads to be constant & reset the time in the domain
loadConst -time 0.0
remove recorders
source WipeOutputFiles.tcl
wipeAnalysis
```

10. Define ground motion time series

```
# define ground motion scale factor
set SF 2.0
```

```
        # read number of points (nPts) and sampling time step (dT) from ground motion
file
        …

        timeSeries Path 101 -dt $dT -filePath $outFile -factor [expr $g*$SF]
        pattern UniformExcitation 101 1 -accel 101
```

11. Recorder generation

```
# create recorder objects
…
```

12. Define dynamic analysis

```
        # Start of analysis generation
        # create the system of equations
        system Mumps
        # create the DOF numberer
        numberer Plain
        # create the constraint handler
        constraints Plain
        # create the integration scheme
        integrator AlphaOSGeneralized 0.9
        # create the solution algorithm
        algorithm Linear
        # create the analysis object
        analysis Transient
```

13. Define analysis time step size

```
        # end time of ground motion
        set Tfinal [expr $dT*$nPts]

        # analysis time step size
        set dtAna [expr 10.0/2048.0]

        # generalized information to be used in time-stepping loops
        set dt $dtAna
        set npts [expr int($Tfinal/$dtAna)]
```

14. Run ground motion record

```
        # record initial state of model
        record

        # open output file for writing
        set outFileID [open $outDIR/elapsedTimeGM.txt w]

        # perform the transient analysis
        set tTot [time {
          for {set i 1} {$i <= $npts} {incr i} {
            set t [time {analyze 1 $dt}]
            puts $outFileID $t
            #puts "step $i"
          }
        }]
        puts "\nElapsed time = $tTot \n"

        # close the output file
        close $outFileID
```

15. Run free vibration, as needed

```
        set tcurr [getTime]
        set Tfree 60.0
```

```
set Tfinal_free [expr $Tfinal+$Tfree]

while {$ok == 0 && $tcurr < $Tfinal_free} {
        set ok [analyze 1 $dt]
        set tcurr [getTime]
}
if {$ok != 0} {
        puts "\n\n----- free vibes convergence failure -----.\n\n"
}
puts "free vibes complete. GM: $gm. Scale: $SF. End Time: [getTime]. Tfinal:
$Tfinal_free."
```

16. Leave analysis open to run wave (e.g., for 100,000,000 steps). Note, the simulation may need to be stopped manually after the wave loading.

```
puts "ready for wave..."

# open output file for writing
set outFileID [open $outDIR/elapsedTimeWave.txt w]

# perform the transient analysis
set tTot [time {
  for {set i 1} {$i <= 100000000} {incr i} {
        set t [time {analyze 1 $dt}]
        puts $outFileID $t
        #puts "step $i"
  }
}]
puts "\nelapsed time = $tTot \n"

# close the output file
close $outFileID
```

Note: Simulation may require a hard shut down after wave has passed.

17. End of analysis

```
remove recorders
source WipeOutputFiles.tcl
wipeAnalysis
wipeExp
wipe
exit
```

The function for the WipeOutputFiles.tcl to clean up output files after running OpenSeesSP is provided below:

```
# clean up empty output files after running OpenSeesSP
set delFileList [glob -nocomplain "$outDIR/*.out.*"]
#puts "Files to delete: $delFileList"
foreach f $delFileList {
  file delete -force $f
}
```

To troubleshoot MPICH2 installation:

1. Uninstall previous version of MPICH2, as needed.

2. Open an admin command prompt by right-clicking on the command prompt icon and selecting "run as administrator".

3. Run "mpiexec /i mpich2-1.3.2p1-win-ia32.msi" (or any version needed) from the admin command prompt to install MPICH2.

4. During installation select that MPICH2 be installed for "Everyone" for all users.

5. Run wmpiconfig and store username/password.

6. Add "C:\Program Files\MPICH2\bin" to system Path and reboot.

7. Check smpd using 'smpd -status' (should return 'smpd running on $hostname$', e.g., simulinkrt-host/simpsoba-host).

8. To test execution environment, go to the directory $MPICHROOT\examples and run cpi.exe using: 'mpiexec -n 4 cpi'.